

A search for ionized jets towards massive young stellar objects

S. J. D. Purser,¹★ S. L. Lumsden,¹ M. G. Hoare,¹ J. S. Urquhart,^{2,3} N. Cunningham,^{1,4}
C. R. Purcell,⁵ K. J. Brooks,⁶ G. Garay,⁷ A. E. Gúzman⁷ and M. A. Voronkov⁶

¹*School of Physics and Astronomy, University of Leeds, Leeds LS2 9JT, UK*

²*Max-Planck-Institute für Radioastronomie, Auf dem Hügel 69, D-53121 Bonn, Germany*

³*Centre for Astrophysics and Planetary Science, The University of Kent, Canterbury, Kent CT2 7NH, UK*

⁴*National Radio Astronomy Observatory, PO Box 2, Green Bank, WV 24944, USA*

⁵*Sydney Institute for Astronomy (SIfA), School of Physics, The University of Sydney, NSW 2006, Australia*

⁶*Australia Telescope National Facility, CSIRO Astronomy and Space Science, PO Box 76, Epping, NSW 1710, Australia*

⁷*Departamento de Astronomía, Universidad de Chile, Casilla 36-D, Santiago, Chile*

Accepted 2016 April 28. Received 2016 April 4; in original form 2016 January 26

ABSTRACT

Radio continuum observations using the Australia telescope compact array at 5.5, 9.0, 17.0 and 22.8 GHz have detected free–free emission associated with 45 of 49 massive young stellar objects and H II regions. Of these, 26 sources are classified as ionized jets (12 of which are candidates), 2 as ambiguous jets or disc winds, 1 as a disc-wind, 14 as H II regions and 2 were unable to be categorized. Classification as ionized jets is based upon morphology, radio flux and spectral index, in conjunction with previous observational results at other wavelengths. Radio luminosity and momentum are found to scale with bolometric luminosity in the same way as low-mass jets, indicating a common mechanism for jet production across all masses. In 13 of the jets, we see associated non-thermal/optically thin lobes resulting from shocks either internal to the jet and/or at working surfaces. 10 jets display non-thermal (synchrotron emission) spectra in their lobes, with an average spectral index of $\alpha = -0.55$ consistent with *Fermi* acceleration in shocks. This shows that magnetic fields are present, in agreement with models of jet formation incorporating magnetic fields. Since the production of collimated radio jets is associated with accretion processes, the results presented in this paper support the picture of disc-mediated accretion for the formation of massive stars with an upper limit on the jet phase lasting approximately 6.5×10^4 yr. Typical mass-loss rates in the jet are found to be $1.4 \times 10^{-5} M_{\odot} \text{ yr}^{-1}$ with associated momentum rates of the order of $(1-2) \times 10^{-2} M_{\odot} \text{ km s}^{-1} \text{ yr}^{-1}$.

Key words: stars: evolution – stars: formation – stars: massive – stars: protostars – ISM: jets and outflows – radio continuum: ISM.

1 INTRODUCTION

The formation of massive stars still presents a problem in astrophysics today. With their powerful outflows and radiative outputs, they play a significant role in local (cloud/clump scale) as well as Galactic evolution, thus understanding massive young stellar objects (MYSOs) and their formation is of critical importance. Current theories on the exact mechanisms of formation include the incorporation of accretion through discs (McKee & Tan 2002), similar to the low-mass paradigms of Shu, Adams & Lizano (1987), as well as a competitive accretion scenario whereby the size of the reservoir of accreted material on to an MYSO’s disc stems from the gravitational potential in which it resides (Bonnell et al. 2001). Due to sampling/observational constraints (a by-product of the compara-

tive rarity and extreme distances of massive stars), only a few cases of accretion discs around massive stars have been observed (e.g. Cep A HW2, HH 80-81; Patel et al. 2005; Carrasco-González et al. 2012, respectively), most notably the disc imaged through near-infrared interferometry by Kraus et al. (2010) around the MYSO, IRAS 13481–6124 (G310.0135+00.3892 in this paper). With the advent of Atacama Large Millimeter Array (ALMA) however, we expect this type of observation to become more common. One such example is that of the MYSO G345.4938+01.4677 (Guzmán et al. 2014) which showed evidence in SO₂ molecular lines of a rotating disc structure perpendicularly oriented to the previously established ionized jet (Guzmán, Garay & Brooks 2010).

For this work, we turn our attention towards the larger scale jets of ionized material moving away from, and perpendicular to, the disc. As well as carrying away excess angular momentum (avoiding terminal ‘spin-up’ of the protostar), they also provide a source of momentum to drive/entrain large-scale molecular

* E-mail: pysjp@leeds.ac.uk.

outflows, almost ubiquitously associated with sites of massive star formation (Beuther et al. 2002). With their detection, they provide indirect evidence for the accretion process itself, while measurement of jet velocities, momenta and mass-loss rates (Eisloffel et al. 2000) can provide an insight into the exact accretion mechanisms in operation. In turn, this may aid in differentiating between competitive/Bondi–Hoyle accretion (Bonnell et al. 2001) and turbulent core accretion models (McKee & Tan 2002).

Ideas put forward to explain both the production and collimation of ionized jets from massive stars are based upon those of their low-mass counterparts. Mechanisms have been suggested, which can be categorized as either being driven purely in the disc, or by disc/stellar wind interactions.

A pure disc-wind model was produced by Blandford & Payne (1982), who suggested that a poloidal magnetic field originating from the accretion disc itself, would act as a launching mechanism for ionized material travelling inwards in the disc. This material would travel along the field lines and away from the disc, accurately adhering to the analogy of ‘beads on a wire’. As the accretion disc rotates, these field lines become more twisted (due to magnetic coupling) further from the disc and eventually collimation is induced by ‘hoop stresses’ from the field upon the ionized material. Simulations by Seifried et al. (2012) showed that massive protostellar jets were likely driven by this mechanism, with varying hoop stresses (enhanced by weaker magnetic fields, and suppressed by sub-Keplerian disc motions in the presence of strong fields) in the disc affecting the degree of collimation. This result predicted that collimation should relate to the evolutionary stage of the MYSO, with lower degrees of collimation for younger MYSOs. The jet in W75N VLA 2 shows an example whereby the collimation is evolving with time, with collimation increasing with time (Carrasco-González et al. 2015).

On the other hand, Shu et al. (1994) proposed a model involving both stellar, and disc magnetic fields, referred to as the ‘X-wind model’. This is so named because the launching radius for the jet in the disc is located at the X-shaped lines of equipotential (balancing points of gravitational and centrifugal forces) located near the truncated (by strong stellar magnetic fields), inner surface of the disc itself. With the inward flow of material in the accretion disc, magnetic coupling bows the field lines inwards. Consequently, this inflowing material follows these field lines up and away from the disc. Magnetocentrifugal processes accelerate the gas supersonically in a direction parallel to the poloidal field lines, resulting in an outflowing wind. Twisted magnetic fields further away from the disc’s mid-plane focus the ionized material, resulting in a collimated, ionized jet. When applied to massive star formation, the X-wind model presents a problem however. Stellar magnetic fields are intrinsically related to the convective nature of their protostars. For low-mass protostars, these convective models adhere well to reality with the onset of deuterium burning (Stahler 1988). Simulations of the protostellar evolution of MYSOs (e.g. Hosokawa & Omukai 2009) show them to evolve through radiative as well as convective stages, so this phase is much more limited in time.

The observation by Carrasco-González et al. (2010) of polarized emission from an ionized jet associated with the HH 80-81 object, revealed possible poloidal field lines, suggesting a magnetic mechanism for jet formation around MYSOs. However, this type of result is not common in the literature, and the formation of jets around massive protostars is still an open question.

Observationally, much information can be gleaned from measurement of the spectral index of a jet’s free-free radio emission.

A paper by Reynolds (1986) derived the following relationships between a jet’s physical parameters:

$$\alpha = 2 + \frac{2.1}{q_\tau} (1 + \epsilon + q_T) \quad (1)$$

$$\alpha = \frac{4\beta - 6.2}{2\beta - 1}, \quad (2)$$

where α is the spectral index ($S_\nu \propto \nu^\alpha$), ϵ represents the degree of collimation and q_T and q_τ are essentially the powers to which the temperature and optical depth in the jet vary with distance from the base of the jet. For equation (2), $n_e \propto r^{-\beta}$ where n_e is the number density of electrons, and r is the distance from the MYSO.

For a standard (i.e. not accelerating or recombining) bi-conical jet, a spectral index of ~ 0.6 is expected, however spectral indices of $-0.1 \rightarrow 1.6$ are found when considering a variety of jet scenarios. Although the derivation of the spectral index cannot be used to infer temperature or density profiles along the jet, we can deduce information about the jet’s geometry (collimation) and processes likely ongoing within the flow (such as further acceleration or recombination for example), as summarized in table 1 of Reynolds (1986). As well as the spectral index, we can measure the behaviour of the deconvolved major axis of the jet with frequency (which is dependent upon the relationship between electron density and radial distance from the powering source), i.e. $\theta_{\text{maj}} \propto \nu^\gamma$, where θ_{maj} is the deconvolved major axis and γ is the measured index. For a conical wind ($\alpha = 0.6$), we expect $\gamma = -0.7$ as can be seen from equations (2) and (3), demonstrating the connection between these two variables,

$$\gamma = -\frac{2.1}{2\beta - 1}. \quad (3)$$

Specific examples of radio jets in the literature, associated with sites of high-mass star formation, are those of HH 80-81 (G010.8411–02.5919) and Cepheus HW-2. These MYSOs harbour thermal jets found to have proper motions of ~ 500 and ~ 480 km s $^{-1}$ (Martí, Rodríguez & Reipurth 1998; Curiel et al. 2006, respectively), which are much greater than the velocities typically seen in low-mass cases of ~ 200 km s $^{-1}$ (Arce et al. 2007). Interestingly, even larger velocities were reported for other parts within the HH 80-81 jet of 600–1400 km s $^{-1}$ in an earlier study (Martí, Rodríguez & Reipurth 1995). Cepheus HW-2 consists of a simple elongated structure with a spectral index of $\alpha = 0.69 \pm 0.06$, indicative of a conical bipolar jet (Rodríguez et al. 1994). Conversely HH 80-81 consists of a more complex picture whereby a central, thermal source ($\alpha \sim 0.2$) and two non-thermal lobes ($\alpha \sim -0.3$) align on a NE-SW orientation (Martí, Rodríguez & Reipurth 1993). These two examples show the range of complexities which radio observations of ionized jets reveal.

Systematic searches for ionized jets are few and far between, and conducted with sporadic success. Gibb & Hoare (2007) performed radio observations from 5 to 43 GHz towards five MYSOs with spectral indices ranging from 0.2 to 0.8, all consistent with ionized jets/winds (Reynolds 1986). Although no jets were definitively identified, two sources (S106-IR and S140-IRS1), whose radio emission was perpendicular to their associated molecular outflows, were classified as equatorial disc winds. Another survey by Guzmán et al. (2012) detected two radio jets (G343.1261–00.0623 and G345.4938+01.4677 in this paper) from a sample of 33 (8 of which were observed) IR-luminous objects taken, in part, from the Red MSX Source (RMS) survey (see Section 2.1). An issue with this survey’s sampling methodology was selection criteria based upon positive radio spectral indices and low radio to IR

luminosities, the radio data which was taken from Walsh et al. (1998) and Urquhart et al. (2007). This resulted in contamination of the sample by unresolved, optically thick H II regions with low radio fluxes, which were underluminous compared to radio fluxes expected from the bolometric luminosities (for an optically thin H II region). The survey's 4σ detection limits were ~ 0.8 mJy, at 1.4 and 2.4 GHz and ~ 0.4 mJy, at 4.8 and 8.6 GHz. Since we expect radio-weak, thermal spectra from the ionized jets, at those frequencies emission from such objects may have remained undetected. Most recently Moscadelli et al. (2016) selected a subsample of MYSOs (zero-age main sequence – ZAMS – type B3-O7) from the Bar and Spiral Structure Legacy (BeSSeL) survey, which displayed water maser activity, and previous compact (< 1 arcsec), and weak (which they define as < 50 mJy) radio emission. Of the 40 objects in the sample, 11 were observed with the VLA at *C*, *K* and *Ku* bands ($\theta_{\text{res}} \sim 0.2$ arcsec), 10 displayed spectral indices typical of thermal jets, 5 of which were confirmed to have collimated (opening angles, θ_0 , of between 10° and 30°) outflows via maser kinematics. Spectral indices ranged between $0.1 \leq \alpha \leq 1.1$, with inferred momentum rates of between 10^{-3} and $1 M_\odot \text{ km s}^{-1} \text{ yr}^{-1}$. Interestingly, lobes of elongated, non-thermal emission were observed towards two of the sample, suggestive of both particle-acceleration and the presence of magnetic fields.

With these previous ionized jet surveys in mind, our own RMS survey-derived selection of targets, in conjunction with the targets of Guzmán et al. (2012), was used to create an unbiased sample of MYSOs which could harbour ionized jets.

In this paper, we introduce the methodology of our sample selection (Section 2), and explain the technicalities of its observation in Section 3.1. Section 4 contains a discussion of cleaned and imaged radio data (Fig. C1 in the online version) and their relation to previous observations within the literature. This is done for a selection of specific examples representative of the sample as a whole. An overall, statistical approach is then employed in Section 5, from which implications to current jet and accretion models are discussed. These findings are summarized in Section 6.

2 A SAMPLE OF MYSOS

2.1 The RMS survey

The RMS survey (Lumsden et al. 2013) is a systematic search for MYSOs using previous surveys as well as mm, radio and infrared follow-up observations to aid in the classification of objects catalogued by the Mid-course Space eXperiment (MSX; Price et al. 2001). This extensive, ordered approach was necessary considering the relative sparsity of forming massive stars in the Galaxy.

In order to extract genuine MYSO candidates from the MSX data base, contaminant objects such as planetary nebulae, old dusty stars and resolved ultracompact H II regions had to be removed. Since most of the bolometric luminosity of an MYSO lies at infrared wavelengths (due to dust reprocessing), a comparison of fluxes at a variety of IR-wavelengths (based on known MYSOs) was employed. The exact sampling methodologies used can be found in Lumsden et al. (2002).

VLA (Urquhart et al. 2009a) and Australia Telescope Compact Array (ATCA; Urquhart et al. 2007) observations at 5 GHz ($\theta_{\text{res}} \sim 1$ arcsec) helped to remove compact UCHIIs, while mm observations by MOPRA ($^{13}\text{CO}(1-0)$) and James Clerk Maxwell Telescope (JCMT) ($^{13}\text{CO}(2-1)$) allowed the removal of close, low-mass YSOs by the determination of kinematic distances and therefore absolute luminosities (Urquhart et al. 2007). The relative strength of the CO

lines helped eliminate dusty, evolved stars (stronger in young stars) while those evolved stars lying along the line of sight to H₂ molecular clouds were picked out on the basis of their distinct near-IR absorption spectra.

The resulting RMS data base¹ catalogues ~ 900 embedded, young massive stars (Urquhart et al. 2014a) of which both H II regions and MYSOs are included.

2.2 Sample selection

In total, we have a sample of 49 individual objects which are listed in Table 1. Of these, 34 were selected to form a distance-limited (DL; $d < 7$ kpc) sample of MYSOs. An even spread in the luminosities of the objects was required for unbiased sampling in terms of bolometric luminosity and consequently six of these objects fall in the range $700 L_\odot \leq L_* < 3000 L_\odot$, 11 in the range $3000 L_\odot \leq L_* \leq 10000 L_\odot$, 9 in the range $10000 L_\odot \leq L_* \leq 30000 L_\odot$ and 8 with $L_* > 30000 L_\odot$. It is worth noting that derived bolometric luminosities have changed for some of the sample since the observations. The previous observations of Urquhart et al. (2007) have demonstrated them all to be radio weak with $S_\nu < 2$ mJy. These sources are at elevations conducive to more circular synthetic apertures, whereby $\delta < -34^\circ$. Targets with declinations greater than the quoted cut-off have been included due to their scientific value, as well as filler objects for allocated times when the other sources were not fully risen above the horizon (i.e. elevation $< 20^\circ$). Further eight objects were added to complete the observations (at 17 and 22.8 GHz) which Guzmán et al. (2012) performed from 1.4 to 8.6 GHz with the ATCA. One of the Guzman sample (G317.4298–00.5612) was observed at 5 and 9 GHz to check for variability. Four of the objects were added on the basis of being associated with $4.5 \mu\text{m}$ excesses, or extended green objects (EGOs; Cyganowski et al. 2008), a signature of shocks possibly caused by jet activity (Smith & Rosen 2005). The latter two samples were not DL and also were used to fill in coverage in right ascension.

3 OBSERVATIONS AND DATA REDUCTION

3.1 Radio observations with the ATCA

All radio observations were made using the ATCA (see chapter 1, section 1 of Frater, Brooks & Whiteoak 1992, for an overview) in the 6A and 6B configurations, over a period of 12 d, spread over 4 yr. A total of 49 individual, compact objects were observed at four different frequency bands (centred on 5.5, 9.0, 17.0 and 22.8 GHz). These frequencies were observed using a bandwidth of 2048 MHz (XX, YY, XY, and YX polarizations) split evenly either side of the central frequencies (an overview of the Compact Array Broadband Backend (CABB) correlator's capabilities can be found in Wilson et al. 2011). This bandwidth was split into channels of width 1 MHz (minimizing the averaging out effect of Radio Frequency Interference (RFI) over broad channels and giving the ability to easily recognize and flag it). From this point on, the frequency bands observed shall be referred to as 5.5, 9, 17 and 22.8 GHz bands.

The highest frequency band has been also chosen to incorporate the H₂O(6 \rightarrow 5) transition at 22.235 GHz, in order to observe masing activity and allow more accurate, phase-only self-calibration from the relevant channels.

¹ http://rms.leeds.ac.uk/cgi-bin/public/RMS_DATABASE.cgi

Table 1. Target sources observed by ATCA between 12/02/2010 and 28/02/2013, their bolometric luminosities and distances (Lumsden et al. 2013). Sample selection is indicated by the superscripted symbol on each source's name, whereby \star indicates a filler object of scientific value, \dagger indicates an object which is part of the Guzmán et al. (2012) sample and \ddagger indicates an MYSO associated with an EGO (Cyganowski et al. 2008). Any source without a symbol is part of the DL sample. The footnote marks for the distances indicate how they were calculated: (a) kinematic distance determined using the source velocity; (b) spectrophotometric distance; (c) maser parallax distance; (d) distances taken from the literature. The footnote marking for the bolometric luminosities show the relevant calculation methods which were: (a) spectral energy distribution (SED) fit to the available infrared fluxes (e.g. 2MASS, MSX) including HiGAL (Mottram et al., in preparation); (b) SED fit to infrared and either MIPS GAL 70 μm or IRAS Galaxy ATLAS 60 μm fluxes (Mottram et al. 2010, 2011); (c) MSX 21 μm band flux using a scaling relationship determined from a comparison with sources where SED fits have been possible (Mottram et al. 2011). Also included are the epochs during which their data was recorded by the ATCA for the 5.5/9 GHz setup and 17/22.8 GHz setup. The epoch notation corresponds to the following dates: E1, 12/02/2010-13/02/2010; E2, 16/04/2011; E3, 10/09/2011-11/09/2011; E4, 05/01/2012-07/01/2012; E5, 25/02/2013-28/02/2013. Date ranges include all dates in between those provided. Hyphenated table cells denote the source not being observed at the relevant frequencies. The final column denotes each object's final classification, whereby H II regions follow the accepted acronyms, N/D indicates a non-detection, U/K indicates where no robust classification could be made, DW indicates a disc-wind, while Jet/DW indicates an ambiguous classification and the presence of an (L) and/or (C) after 'jet' indicates whether lobes were present and/or the object was only classified as a jet candidate, respectively.

Object name	Associated object	RA (J2000)	Dec. (J2000)	D (kpc)	L_{Bol} (L_{\odot})	5.5/9 (GHz)	17/22.8 (GHz)	Class.
G010.8411–02.5919 \star	IRAS 18162–2048	18 ^h 19 ^m 12 ^s .09	–20°47′30″.90	1.9 ^a	2.40 \times 10 ^{4b}	–	E2	Jet
G012.9090–00.2607 \star	IRAS 18117–1753	18 ^h 14 ^m 39 ^s .56	–17°52′02″.30	2.4 ^c	3.20 \times 10 ^{4a}	–	E3	Jet (C)
G014.9958–00.6732 \star	–	18 ^h 20 ^m 19 ^s .47	–16°13′29″.80	2.0 ^c	1.30 \times 10 ^{4c}	–	E3	Jet (C)
G251.2337–01.9535	IRAS 08008–3423	08 ^h 02 ^m 42 ^s .97	–34°31′48″.70	4.6 ^a	8.20 \times 10 ^{3a}	E5	E4	Jet (C)
G254.0491–00.5615	IRAS 08140–3559	08 ^h 15 ^m 57 ^s .12	–36°08′06″.80	3.0 ^a	1.70 \times 10 ^{3a}	E5	E1	Jet
G254.0548–00.0961	IRAS 08159–3543	08 ^h 17 ^m 52 ^s .62	–35°52′47″.60	2.8 ^a	1.90 \times 10 ^{3a}	E5	E1	Jet (L)
G263.2283+01.5712	IRAS 08513–4201	08 ^h 53 ^m 09 ^s .46	–42°13′07″.60	0.7 ^d	1.20 \times 10 ^{3b}	E5	E1	Jet
G263.7434+00.1161	IRAS 08470–4321	08 ^h 48 ^m 48 ^s .64	–43°32′29″.00	0.7 ^d	1.20 \times 10 ^{3a}	E5	E1	Jet (L)
G263.7759–00.4281	IRAS 08448–4343	08 ^h 46 ^m 34 ^s .84	–43°54′29″.80	0.7 ^d	1.30 \times 10 ^{3a}	E5	E1	Jet (L)
G265.1438+01.4548	RCW 36	08 ^h 59 ^m 27 ^s .40	–43°45′03″.70	0.7 ^d	7.19 \times 10 ^{2c}	–	E1,E4	Jet/DW
G268.3957–00.4842	IRAS 09017–4716	09 ^h 03 ^m 25 ^s .08	–47°28′27″.50	0.7 ^d	3.00 \times 10 ^{3a}	–	E1	N/D
G274.0649–01.1460A	–	09 ^h 24 ^m 42 ^s .54	–52°01′50″.60	5.7 ^a	6.00 \times 10 ^{3a}	E5	E4	HCHII
G282.2988–00.7769	IRAS 10082–5647	10 ^h 10 ^m 00 ^s .32	–57°02′07″.30	3.7 ^a	4.00 \times 10 ^{3b}	–	E1	N/D
G283.9146–01.0485	–	10 ^h 18 ^m 49 ^s .96	–58°10′11″.30	4.9 ^a	6.00 \times 10 ^{3a}	–	E1	N/D
G284.2438–01.1302	IRAS 10187–5810	10 ^h 20 ^m 35 ^s .17	–58°25′07″.10	4.2 ^a	4.40 \times 10 ^{3a}	E5	E1	CHII
G286.2086+00.1694	IRAS 10365–5803	10 ^h 38 ^m 32 ^s .70	–58°19′14″.30	2.3 ^a	8.00 \times 10 ^{3a}	–	E1	Jet (L,C)
G287.3716+00.6444	IRAS 10460–5811	10 ^h 48 ^m 04 ^s .55	–58°27′01″.50	4.5 ^a	1.80 \times 10 ^{4b}	E5	E1	CHII
G298.2620+00.7394	IRAS 12091–6129	12 ^h 11 ^m 47 ^s .68	–61°46′18″.80	4.0 ^a	1.50 \times 10 ^{4a}	E5	E3	DW
G300.9674+01.1499 \dagger	IRAS 12320–6122	12 ^h 34 ^m 53 ^s .22	–61°39′40″.00	4.3 ^a	4.50 \times 10 ^{4c}	–	E4	UCHII
G301.1364–00.2249 \dagger	IRAS 12326–6245	12 ^h 35 ^m 35 ^s .13	–63°02′31″.60	4.3 ^a	3.80 \times 10 ^{5a}	–	E3	HCHII
G305.1940–00.0051 \ddagger	–	13 ^h 11 ^m 14 ^s .44	–62°47′25″.50	4.0 ^b	7.00 \times 10 ^{3a}	E5	–	N/D
G305.2017+00.2072A	IRAS 13079–6218	13 ^h 11 ^m 10 ^s .45	–62°34′38″.60	4.0 ^b	3.00 \times 10 ^{4b}	–	E4	U/K
G305.5610+00.0124	IRAS 13111–6228	13 ^h 14 ^m 26 ^s .36	–62°44′30″.40	4.0 ^b	1.20 \times 10 ^{4a}	E5	E4	HCHII
G308.9176+00.1231A	IRAS 13395–6153	13 ^h 43 ^m 01 ^s .70	–62°08′51″.20	5.3 ^a	9.00 \times 10 ^{4a}	–	E4	UCHII
G310.0135+00.3892	IRAS 13481–6124	13 ^h 51 ^m 37 ^s .85	–61°39′07″.50	3.2 ^a	6.70 \times 10 ^{4a}	E5	E3	Jet (L)
G310.1420+00.7583A	IRAS 13484–6100	13 ^h 51 ^m 58 ^s .27	–61°15′41″.70	5.4 ^a	8.00 \times 10 ^{3a}	E5	E4	Jet (L)
G313.7654–00.8620 \ddagger	IRAS 14212–6131	14 ^h 25 ^m 01 ^s .53	–61°44′57″.60	7.8 ^a	6.10 \times 10 ^{4a}	E5	–	Jet (L)
G317.4298–00.5612 \dagger	IRAS 14477–5947	14 ^h 51 ^m 37 ^s .59	–60°00′19″.40	14.2 ^a	3.50 \times 10 ^{5a}	E5	–	HCHII
G317.8908–00.0578 \dagger	IRAS 14492–5908	14 ^h 53 ^m 06 ^s .16	–59°20′59″.40	13.6 ^a	6.30 \times 10 ^{4a}	–	E2	UCHII
G318.9480–00.1969A	–	15 ^h 00 ^m 55 ^s .31	–58°58′52″.60	2.4 ^a	1.00 \times 10 ^{4a}	E5	E3	Jet/DW
G326.6618+00.5207	IRAS 15412–5359	15 ^h 45 ^m 02 ^s .84	–54°09′03″.00	1.8 ^b	1.40 \times 10 ^{4a}	E5	E2	Jet (C)
G327.1192+00.5103	IRAS 15437–5343	15 ^h 47 ^m 32 ^s .80	–53°52′39″.30	4.9 ^a	3.70 \times 10 ^{4a}	E5	E2	Jet
G331.3576+01.0626	IRAS 16026–5035	16 ^h 06 ^m 25 ^s .78	–50°43′22″.00	4.5 ^a	1.80 \times 10 ^{4a}	E5	E3	Jet (C)
G331.5414–00.0675 \ddagger	–	16 ^h 12 ^m 09 ^s .00	–51°25′47″.00	5.0 ^a	6.00 \times 10 ^{4a}	E5	–	UCHII
G332.0939–00.4206	IRAS 16124–5110	16 ^h 16 ^m 16 ^s .46	–51°18′25″.20	3.6 ^b	9.30 \times 10 ^{4a}	E5	E2	Jet (L)
G332.8256–00.5498A	IRAS 16164–5046	16 ^h 20 ^m 11 ^s .06	–50°53′16″.20	3.6 ^b	1.30 \times 10 ^{5a}	E5	E2	UCHII
G332.9868–00.4871	RCW 106	16 ^h 20 ^m 37 ^s .81	–50°43′49″.60	3.6 ^b	1.80 \times 10 ^{4a}	E5	E4	Jet (C)
G337.8442–00.3748 \dagger	IRAS 16367–4701	16 ^h 40 ^m 26 ^s .68	–47°07′13″.10	3.0 ^a	3.70 \times 10 ^{4a}	–	E2	HCHII
G338.9196+00.5495	–	16 ^h 40 ^m 34 ^s .04	–45°42′07″.90	4.2 ^a	3.20 \times 10 ^{4b}	E5	E3	Jet (C)
G339.6221–00.1209	IRAS 16424–4531	16 ^h 46 ^m 05 ^s .99	–45°36′43″.90	2.8 ^a	1.90 \times 10 ^{4a}	E5	–	Jet (L,C)
G339.8838–01.2588	IRAS 16484–4603	16 ^h 52 ^m 04 ^s .66	–46°08′33″.60	2.7 ^a	6.40 \times 10 ^{4b}	E5	E2	Jet (L)
G340.0543–00.2437A	IRAS 16445–4516	16 ^h 48 ^m 13 ^s .69	–45°21′42″.50	3.8 ^a	2.90 \times 10 ^{4a}	E5	–	Jet (C)
G340.2480–00.3725 \dagger	IRAS 16458–4512	16 ^h 49 ^m 29 ^s .97	–45°17′44″.40	3.7 ^a	3.40 \times 10 ^{4a}	–	E2	UCHII
G343.1261–00.0623 \dagger	IRAS 16547–4247	16 ^h 58 ^m 17 ^s .20	–42°52′07″.10	2.8 ^a	1.90 \times 10 ^{4a}	–	E2, E4	Jet (L)
G343.5213–00.5171	–	17 ^h 01 ^m 34 ^s .04	–42°50′19″.70	3.2 ^a	6.70 \times 10 ^{3a}	E5	E4	Jet (L,C)
G345.4938+01.4677 \dagger	IRAS 16562–3959	16 ^h 59 ^m 41 ^s .61	–40°03′43″.30	2.4 ^b	1.50 \times 10 ^{5b}	–	E2	Jet (L)
G345.5043+00.3480	IRAS 17008–4040	17 ^h 04 ^m 22 ^s .87	–40°44′23″.50	2.0 ^a	1.00 \times 10 ^{5a}	E5	E4	Jet (C)
G345.9561+00.6123	IRAS 17012–4009	17 ^h 04 ^m 43 ^s .00	–40°13′13″.40	2.5 ^a	2.40 \times 10 ^{3a}	E5	E3	U/K
G348.6972–01.0263 \ddagger	RCW 121	17 ^h 19 ^m 58 ^s .91	–38°58′14″.80	2.8 ^b	1.30 \times 10 ^{5a}	E5	–	UCHII

Table 2. A table of the observable radio recombination lines for each observed band, and the associated resolution per 1 MHz channel (at the centre of each band).

Band (GHz)	RRLs	Δv (km s ⁻¹)
5.5	H100 α –H112 α	54.5
9	H87 α –H93 α	33.3
17	H71 α –H73 α	17.6
22.8	H65 α , H66 α	13.1

Throughout the radio bands, radio recombination lines should also be observable in the strongest sources, giving some degree of kinematic information for the ionized gas. Table 2 shows the radio recombination lines falling within the observed bands, and their effective, velocity resolutions for a channel width of 1 MHz.

The range of scales the instrument was sensitive to were 2.0–16.5 arcsec, 1.2–10.1 arcsec, 0.6–5.4 arcsec and 0.5–4.0 arcsec over the 5.5, 9, 17 and 22.8 GHz frequency bands, respectively. These correspond to a maximum baseline length of 6 km and a minimum of ~ 300 m.

Individual scan times on flux and phase calibrators were 5 min and 90 s, respectively, and on target sources were between 5 and 20 min dependent on atmospheric conditions and observing frequencies. The average total integration time on each science target, τ_{int} , was ~ 75 min. Observations at 5.5 and 9 GHz were all conducted during 2013 February, with a typical rms noise level calculated to be 17 and 20 $\mu\text{Jy beam}^{-1}$, respectively. The upper two frequency bands were observed during the months of 2010 February, 2011 April, 2011 September and 2012 January, giving a range of conditions particularly affecting the 22.8 GHz band which is more sensitive to atmospheric water vapour content (greater during the Southern hemisphere’s summer months). Theoretical rms noise levels therefore range between 40–41 and 73–106 $\mu\text{Jy beam}^{-1}$ for the 17 and 22.8 GHz bands, respectively, during the months of September (lower noise) and January. As a note, the typical values for the rms noise were calculated assuming the removal of 200 channels (100 at each edge of the bandwidth), RFI interference, typical weather during the relevant months, $\delta \sim -50^\circ$ and a robustness of 0.

3.2 Data reduction

For calibrating and cleaning the data, the Multichannel Image Reconstruction Image Analysis and Display (MIRIAD) software package (Sault, Teuben & Wright 1995) was used. For the measurement of various parameters, the Common Astronomy Software Applications (CASA) was implemented (McMullin et al. 2007).

Multifrequency synthesis was used to image the visibility data sets, and at 5.5, 9 and 17 GHz, the multifrequency CLEAN algorithm (MFCLEAN in MIRIAD) was used to account for the variation in intensity distribution with frequency, since the fractional bandwidth is > 12.5 per cent (Sault & Wieringa 1994). In Fourier transforming the data, the visibilities were weighted according to T_{sys} in order to down-weight data taken at times of increased atmospheric instability and thus improve the signal-to-noise ratio (SNR) of the resultant images. This acted to improve the accuracy of recorded fluxes, at the cost of more elongated restoring beams.

Phase only self-calibration was performed on any strong point source (extended sources give erroneous solutions for the limited baseline numbers of the ATCA) in the field of view, and solutions were applied only if they converged over the course of multiple

iterations (in terms of the rms deviations on the gain phases). Time intervals over which to produce calibration solutions took account of the calibrating source’s flux and the frequency of the observations (since the atmosphere is more stable at lower frequencies). At 22.8 GHz, if masing activity was present for the 22.23508 GHz water line, the strongest channel was imaged and used as a model for phase-only self-calibration. Simultaneous amplitude and phase self-calibration was not performed on any of the data sets since there are not enough constraints with 15 baselines to solve for both the real and imaginary parts of the gains.

3.3 Measurement of fluxes and spectral indices

For the clean images of our observed fields, both resolved and unresolved emission had to be measured. Thus, integrated radio flux measurements on sources in the field/pointing centre were performed in one of two ways, dependent on this morphology. For simple (i.e. Gaussian-like, both resolved and compact) morphologies, the CASA task, IMFIT, was used to measure the deconvolved dimensions, positions and fluxes. IMFIT works by the fitting of one/several Gaussian profile(s) to the image plane (from a roughly guessed model), whose properties estimate those of the source. Residual maps of the Gaussian model(s) subtracted from the real emission were consequently inspected to make sure that no components were unaccounted for (i.e. the residual map is ‘noise-like’). For extended and non-Gaussian morphologies, the fluxes were integrated over the 3σ flux area, positions were taken as the peak emission’s location and deconvolved dimensions were measured using equation (4) below,

$$\theta_G = \sqrt{\theta_{\text{source}}^2 - \theta_{\text{beam}}^2}, \quad (4)$$

where θ_G is the deconvolved size of the source, θ_{source} is the measured full width at half-maximum (FWHM) of the source and θ_{beam} is the FWHM of the restoring beam.

The image rms deviation was measured in portions of the field without emission, close to the source (so residual artefacts from the cleaning process, such as side lobes, were included in the noise estimation).

The measurement of spectral indices for each source was performed using least squares fitting algorithms. Errors on the fluxes included those provided by the noise/Gaussian fit parameters in addition to a generally accepted 10 per cent error on the absolute flux calibration of the ATCA. In the case where only two frequencies are present, the spectral index is estimated from the difference between each flux, whose associated error is estimated by combining the fluxes’ errors (plus the previously mentioned 10 per cent) in quadrature. Similar techniques are used for the derivation of the power-law index associated with the variation of major axis length with frequency, γ .

As a note, thermal sources are defined as those possessing a spectral index of $\alpha \geq -0.1$ and are assumed to be dominated by thermal Bremsstrahlung, while non-thermal sources have $\alpha < -0.1$ and are assumed to be dominated by synchrotron emission. We define the optically thin and thick regimes for free-free emission as $-0.1 \leq \alpha \leq 1$ and $1 < \alpha \leq 2$, respectively.

3.4 Flux recovery with the 6 km configuration

As a check, modelling was performed on a synthetic data set in order to calculate how much flux is resolved out at each observing frequency. This is an expected effect of interferometry, since the

shortest baseline (in units of wavelength) increases in size with increasing frequency and consequentially, the array’s scale-sensitivity drops at larger spatial scales.

The synthetic data set was created with the use of the `MIRIAD` task, `UVGEN`, and mirrors the real observations. Total time on target (positioned at the pointing/phase centres) for the fake observations was 90 min, split into five separate 18 min scans with visibility integration times of 5 s. An elevation limit of 30° was imposed (equivalent to a range in hour angle of $-5^{\text{h}} \leq \text{H.A.} \leq 4^{\text{h}}$), and the source declination used (-60°) is conservative (for the sample) in terms of the maximum elevations for scans ($< 60^\circ$). Typical values of the system temperature of 30, 35, 45 and 100 K were used for the 5.5, 9, 17 and 22.8 GHz bands, respectively. For the model, we used a source with a spectral index $\alpha = 0.6$, a major axis index $\gamma = -0.7$, and a total flux (at 5.5 GHz) of 0.4 mJy. This is representative of a typical ionized wind or jet. The major and minor axes at 5.5 GHz were defined as 0.60 arcsec (position angle of 0°) and 0.21 arcsec, respectively, corresponding to an opening angle in the jet of 20° . Restoring beams were oriented at a position angle of 175° , with major axes approximately 30 per cent larger than minor axes.

In Fig. 1, plotted are the model fluxes, the recovered fluxes (through deconvolution with a Gaussian as discussed in Section 3.3) and the derived spectral index/fit. Flux recovered varied between 91 per cent (at 22.8 GHz) and >99 per cent (at 17 GHz). A spectral index of 0.61 ± 0.17 was derived, with a derived value for γ of ~ -0.6 (physical sizes could not be deconvolved at 5.5 and 22.8 GHz). This test of the array’s performance towards the types of object this paper focuses on, shows that the ATCA effectively recovers the flux and spectral index of a typical ionized jet/wind. The deconvolved sizes were not recovered at both the lower (due to SNR) and upper (due to SNR and the small spatial scales involved) frequencies, while errors were approaching 100 per cent of the deconvolved size at 9 GHz. This shows that for low-SNR objects, the deconvolved dimensions may be unreliable, even though the recovered value for γ in this case is reasonably close to the model’s value. Further to this point, the position angles recovered at 9 and 17 GHz ($145^\circ \pm 46^\circ$ and $126^\circ \pm 10^\circ$, respectively) were not in agreement with the model. The major implication of this result for analysis of low radio SNR sources would be upon the credibility of deconvolved position angles, which should not be taken as absolute. Extended sources, such as UCHII regions, will likely not mirror these results.

3.5 Extragalactic radio sources

A study by Jackson (2004) examined the theoretical, radio, AGN population as a function of flux density and angular density. It considered and predicted FRI, FRII and star-forming galaxy populations on the celestial sphere for three flux-density limits ($10 \mu\text{Jy}$ being the highest) at a frequency of 1.4 GHz. From this work, we extrapolate the predicted populations to a conservative 3σ limit ($60 \mu\text{Jy}$ at 5.5/9 GHz, $90 \mu\text{Jy}$ at 17 GHz and $300 \mu\text{Jy}$ at 22.8 GHz) of our study, and further reduce the populations at each frequency in accordance with the observed average spectral index of radio galaxies ($\bar{\alpha} = -0.65$; Bornancini et al. 2010). In Table 3, we have summarized how many radio galaxies we expect to observe for three fields of view.

This estimate shows that even at 5.5 GHz we only expect to observe one radio galaxy, within 5 arcsec of the pointing centre, for every 50 fields of view. Moreover the star-forming galaxy population has been overestimated, since a power law is a rough approximation which overestimates the population. We also assumed

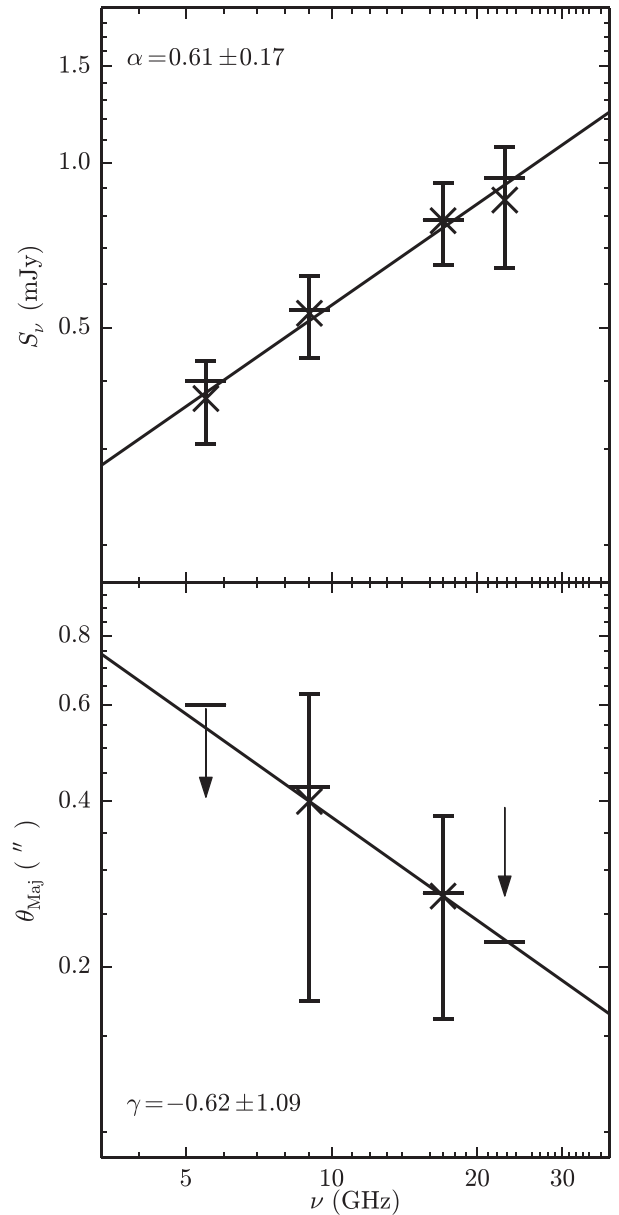


Figure 1. The plotted fluxes (top) and deconvolved major axes (bottom) for both the model (wide horizontal lines) and those recovered through deconvolution with a Gaussian (crosses), for a synthetic data set. The best fits to the measured fluxes and major axes are shown as black lines. Error bars on the recovered fluxes include a 10 per cent absolute flux-scale uncertainty expected from observations using the ATCA. Upper limits on the recovered major axes are also shown. Model parameters used were, $\alpha = 0.6$, $\gamma = -0.7$, $\theta_{\text{Maj}} = 0.6$ arcsec (major axis at 5.5 GHz) and $\theta_{\text{Min}} = 0.21$ arcsec (minor axis at 5.5 GHz).

point-like profiles, however this is not valid for all and likely our observations will resolve many of the closer radio galaxies out, especially at the higher frequencies.

Another study by Anglada et al. (1998) provides extragalactic source number density estimates (their equation A2), which can be extrapolated to other frequencies (using the average spectral index value quoted above). This alternate approach produces number densities ~ 5 times lower than those calculated above across all four frequencies. On this basis, we do not expect this type of object to be a concern for our analysis.

Table 3. Predicted radio galaxy populations, interpolated from the study by Jackson (2004) using simple power laws for each population. For each frequency, different flux-density limits are used (60 μ Jy at 5.5/9 GHz, 90 μ Jy at 17 GHz and 300 μ Jy at 22.8 GHz) typical of our observations.

Type	ν (GHz)	Field of view		
		(1°) ²	(6 arcsec) ²	(10 arcmin) ²
FRI	5.5	222	2.2	0.002
	9.0	161	1.6	0.001
	17.0	88	0.881	0.001
	22.8	41	0.414	<0.001
FR II	5.5	22	0.225	<0.001
	9.0	16	0.163	<0.001
	17.0	9	0.108	<0.001
	22.8	9	0.089	<0.001
Star forming	5.5	1061	11	0.008
	9.0	770	7.7	0.006
	17.0	391	3.9	0.003
	22.8	147	1.5	0.001
Total	5.5	1305	13	0.010
	9.0	947	9.5	0.007
	17.0	488	4.9	0.004
	22.8	197	2.0	0.001

4 RESULTS

We detect emission in 45 of the 49 fields observed. The maps of radio flux are shown in Fig. C1 (online version only) at each observed frequency. For the ionized jets identified (and other associated emission), deconvolved positions are given in Table A1, fluxes/spectral indices are given in Table A2 and sizes/derived values for γ are in Table A3 (these tables are in the online version only). Fluxes, sizes and other derived properties of radio sources identified as H II regions are given in Table A7 (online version only). Any sources that were not part of the sample, but identified within the primary beam of the observations at 5.5 and 9 GHz, have both their fluxes (primary-beam corrected) and positions listed in Table A10 (online version).

4.1 Classification of the radio emission

A high degree of similarity between the different types of object (especially at current resolutions) is, by and large, the main problem and cannot be solved by observations of only one type. In summary, morphology, radio/bolometric flux comparison, radio-spectral features and correlation with previous observations at different wavelengths form the bulk of this process.

An initial inspection of the radio emission’s morphology is usually enough to remove extended H II regions from the sample. For the more compact radio sources (some of which may be embedded in extended emission), a comparison of the measured radio fluxes with those expected from the bolometric luminosities (inferred from the models of Davies et al. 2011) aids in the separation of HCHII and other types of objects. For this study, a cutoff of 20 per cent of the expected radio flux (at the highest observed frequency, thus limiting optical depth effects) was used for identification. A potential pitfall at this point originates from the optical depths towards the prospective H II regions. If still in the optically thick regime (typical for HCHII at the frequencies in this work), the radio flux may be underestimated leading to a false classification as a jet candidate further down the line. Therefore, to avoid an ambiguous classification as a jet/H II region, if strong Br γ emission is seen (from NIR

spectra of Lumsden et al., in preparation), an automatic classification as an H II region is enacted. The 1.644 μ m [Fe II] transition is also of interest as it is indicative of J-type shocks with shock velocities >50 km s⁻¹ (Hollenbach & McKee 1989). These shocks arise from the interaction of the jets with ambient material and therefore the presence of this line within the spectra is taken as evidence of ionized jets or winds.

From the radio flux maps, measurement of both α and γ enables the differentiation between various jet scenarios in accordance with the models of Reynolds (1986, i.e. equations 2 and 3). The deconvolved position angle for the major axis of the jet’s emission is taken to be the jet’s propagation axis, which can then be compared to position angles for molecular outflows present in the literature. In cases whereby the difference between these two position angles is $<45^\circ$ (i.e. parallel), this is taken as enough evidence to warrant classification as a jet. Should this alignment be perpendicular whilst $\alpha \sim 0.6$ and $\gamma \sim -0.7$, a disc wind scenario is deduced. Another indicator in the literature for the outflow axis (to which position angles can be compared) is 2.12 μ m H₂ emission (such as in G310.0135+00.3892; Caratti o Garatti et al. 2015) which is indicative of collisional excitation of molecular hydrogen through shocks attributable to protostellar outflows and/or large Lyman continuum fluxes (Wolfire & Konigl 1991). This emission can arise in both C and J-type shocks, unlike the [Fe II] line.

Optically thin ($\alpha \sim -0.1$, e.g. G345.4938+01.4677; Guzmán et al. 2010) and/or non-thermal lobes of emission ($\alpha < -0.1$, e.g. G343.1261–00.0623; Garay et al. 2003), may be present where the jet shock-ionizes its environment through collisional interaction at working surfaces. The alignment angle of these lobes with the central, thermal jet defines the jet’s axis for which comparison with observations in the literature can be conducted. As with the deconvolved position angles of the thermal jet component, should the derived outflow axis be parallel to molecular outflows and/or 2.12 μ m H₂ emission, this is taken as evidence of a jet and classification as a jet with lobes is made. If perpendicular, classification as a candidate jet with lobes is instead decided.

It is important to emphasize at this point that classification is not an absolute procedure and each case is assessed individually. Although the process presented above provides a robust algorithm in the majority of cases, proper consideration is still required especially in low signal to noise examples where full information cannot be recovered.

4.2 Object results

We report the identification of 28 sources with the characteristics expected of ionized jets, two of which can be identified as either disc-winds or ionized jets (G265.1438+01.4548 and G318.9480–00.1969A). 12 of these jets are given the classification of jet candidate. One source (G298.2620+00.7394) is identified as a disc wind. Of the original sample, 14 H II regions (5 HCHII, 7 UCHII and two compact H II regions) have been identified, with six other UCHII identified in the fields of view for the images. The conditions for classification of the UCHII regions are based on those of Wood & Churchwell (1989). It is also important to note that in cases where there is no clear cut distinction, based upon radius and emission measure, the measured radius of the H II region takes precedence in the classification process.

Four of the sources were not detected at any observing frequency (G268.3957–00.4842, G282.2988–00.7769, G283.9146–01.0485, and G305.1940–00.0051). Fig. 2 shows 1

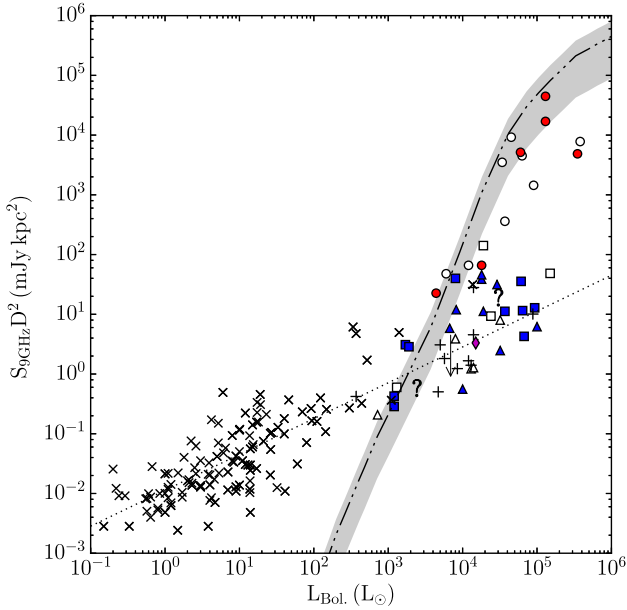


Figure 2. A plot of the 9 GHz distance–luminosities against bolometric luminosity for all detected objects (apart from non-thermal lobes) in the sample. Circles (red) represent H II regions, squares (blue) represent ionized jets, diamonds (magenta) represent disc-winds, triangles (blue) represent jet candidates and ‘x’ markers mark low-mass cases normalized to 9 GHz (assuming $\alpha = 0.6$; Anglada 1995; Furuya et al. 2003; Scaife et al. 2011; Ainsworth et al. 2012). Filled (coloured online) symbols show cases where the flux has been directly measured at 9 GHz, while hollow symbols show cases where the flux has been interpolated from measured spectral indices and higher frequency observations. The ‘+’ symbols represent the sample of high-mass jets from Moscadelli et al. (2016). Lower limits ($<3\sigma$) of non-detections are shown. The dot–dashed line represents the ionized flux expected from the Lyman continuum, taken from stellar models by Davies et al. (2011) for $L_{\text{Bol}} > 10^3 L_{\odot}$, and Thompson (1984) for $L_{\text{Bol}} \leq 10^3 L_{\odot}$. Grey shading represents the area where the radio luminosity is between 20 and 180 per cent of that expected from the bolometric luminosity (for an H II region). The dotted line represents the empirical relation derived for the low-mass case (Anglada 1995), normalized to 9 GHz (assuming $\alpha = 0.6$).

(which was observed at 9 GHz) of the four non-detections as a lower limit, which lies above the flux expected from an ionized jet.

Two objects evaded classification, G305.2017+00.2072A and G345.9561+00.6123. G305.2017+00.2072A imaging displayed evidence of extended, resolved out emission towards the object complicating its deconvolution. Removing shorter baselines did not help to improve the images significantly. Although a faint, compact component was present at 17 GHz coincident with both the MSX point source position and a 6.7 GHz methanol maser, it was not detected at 22.8 GHz and thus no spectral index could be derived. With a bolometric luminosity of $2.4 \times 10^3 L_{\odot}$, G345.9561+00.6123 is one of the less luminous MYSOs in the sample. For the radio emission from an optically thin H II region, a value for $S_{9\text{GHz}} D^2$ (see Section 5.1) of 1.6 mJy·kpc² is expected for $L_{\text{Bol}} = 2400 L_{\odot}$, the measured value being (0.56 ± 0.13) mJy·kpc² at 9 GHz and (1.75 ± 0.44) mJy·kpc² at 17 GHz. Either this may represent an optically thin (at 17 GHz or above), small, emergent H II region or an ionized jet with a large range of possible spectral indices, hence why it remains unclassified.

In summary, the objects reported here have had their classifications tabulated in Table 4.

Table 4. A summary of the numbers and types of objects within the sample, as well as their incidence rate with water masers in the 22.8 GHz band (which takes account of which sources were observed at 22.8 GHz and which were not).

Type	Subtype	Count	Masers?	(per cent)
Ionized jet	With lobes	10	7	78
	w/o lobes	4	2	50
Ionized jet (C)	With lobes	3	1	50
	w/o lobes	9	4	50
Jet/disc wind	–	2	1	50
Disc wind	–	1	0	0
H II region	HCHII (embedded)	3	1	50
	HCHII (isolated)	2	1	50
	UCHII	7	5	100
	Compact H II	2	1	50
Unknown	–	2	0	0
Non-detection	–	4	–	–

Table 5. A summary values for the Kendall–Tau coefficient of correlation, the associated p -value, for both the D/L sample of detected jets and all jets detected (the second column). Presence of (J) next to the sample type denotes jet classifications only, while the absence denotes jets and candidate jets. The size of each sample is tabulated in the third column. τ_p represents the partial Kendall–Tau correlation coefficient and the associated p -value (p_p), whilst controlling for distance.

(x, y)	S	n	τ	p	τ_p	p_p
$(L_{\text{Bol}}, S_{\nu} D^2)$	D/L (J)	10	0.674	0.007	0.479	0.023
	versus D/L	22	0.418	0.006	0.294	0.062
$(M_{\text{Cl}}, S_{\nu} D^2)$	All (J)	14	0.552	0.006	0.479	0.023
	All	28	0.423	0.002	0.351	0.010
	versus D/L	14	0.626	0.002	0.548	0.009
$(M_{\text{Cl}}, S_{\nu} D^2)$	D/L (J)	05	0.800	0.050	0.802	0.102
	versus D/L	14	0.626	0.002	0.548	0.009
	All (J)	08	0.643	0.026	0.645	0.042
	All	17	0.603	<0.001	0.551	0.039
$(M_{\text{Cl}}, M_{\text{Jet}})$	D/L (J)	05	0.400	0.327	0.535	0.276
	versus D/L	14	0.473	0.019	0.476	0.023
$(L_{\text{Bol}}, F_{\text{Jet}})$	All (J)	08	0.357	0.216	0.382	0.228
	All	17	0.485	0.007	0.486	0.009
	versus D/L	10	0.809	0.001	0.742	0.005
$(L_{\text{Bol}}, F_{\text{Jet}})$	D/L	21	0.600	<0.001	0.550	<0.001
	All (J)	14	0.818	<0.001	0.796	<0.001
All	25	0.617	<0.001	0.586	<0.001	

5 ANALYSIS AND DISCUSSION

The analyses presented in this section make use of the Kendall–Tau rank correlation test (Kendall 1938) in order to examine the degree of correlation between various observables. It is used on the basis that it is a non-parametric test, making no assumptions of underlying distributions. Results for each of the correlations presented throughout this section are summarized in Table 5. For consistency, we initially calculate the Kendall–Tau correlation coefficient for measured flux (not distance-flux, $S \cdot D^2$) with distance to be $\tau = 0.18$ with a p -value of 0.38, showing an absence of a Malmquist bias in the DL sample. For fitting the data, we assume a simple power law and use the method of least squares.

5.1 Radio luminosity versus bolometric luminosity

Using the parameters of stellar atmospheres reported in Davies et al. (2011, for $L_{\text{Bol}} > 10^3 L_{\odot}$), it is possible to infer both the spectral type, and UV photon flux, of a ZAMS star with a specific

bolometric luminosity. Since the Lyman flux is intrinsically associated with the amount of material which a young protostar can ionize, we can infer the (optically thin) radio continuum flux expected from an optically thin H II region produced by such a UV flux. Therefore, using this expected radio flux from the bolometric luminosities of the objects, can help to distinguish between H II regions and less evolved phases of massive star formation (see Section 4.1). The specific radio luminosity expected for ionized jets and winds is not as easy to constrain, due to a lack of theoretical models which incorporate all the variables likely influencing the radio luminosity of jets. Therefore, in order to provide us with an idea of the fluxes expected of these objects, we look towards the empirical relations of radio luminosity against bolometric luminosity, $S_{\nu}D^2 \simeq 10^{-2.1} L_{\text{Bol}}^{0.6}$, derived by Anglada (1995). As this relation is derived from a low-mass sample with a maximum bolometric luminosity of $\sim 500 L_{\odot}$, it serves as a comparison for the fluxes we expect to see for thermal jets from MYSOs. Should the mechanism for ionization/jet production be different to the models of shock-ionization (Curiel, Canto & Rodriguez 1987), we should expect to see a deviation towards the higher masses of the MYSOs.

Fig. 2 shows structure attributable to the clear divide between the bright, H II regions near the expected Lyman-continuum line and the jet-like objects which are not as bright as expected from their bolometric luminosities. The H II regions which occupy radio luminosities similar to those of the jets are either resolved out extended regions (higher bolometric luminosities), or are small HCHII regions around lower bolometric luminosity objects. Those H II regions which have lower than expected radio fluxes are usually still in the optically thick regime. It is worth noting that we also expect to see lower radio luminosities for the H II regions than expected from the models of Davies et al. (2011), due to significant dust absorption of Lyman continuum photons (Wood et al. 1988).

The jets themselves can be fitted (DL sample) with a power law with an index of 0.63 ± 0.21 ($\tau = 0.67$, p -value = 0.007). Fitting all jets/candidate (28 sources) yields an index value of 0.75 ± 0.17 . We must add that fitting the low-mass jet sample of Anglada (1995) with the same algorithms as employed upon our high-mass sample yields a higher coefficient of 0.67 ± 0.10 ($\tau = 0.55$, p -value < 0.001) than that recorded by Anglada (1995). When fitting both the high-mass and low-mass sample of jets together, we arrive at a coefficient value of 0.64 ± 0.04 ($\tau = 0.73$, p -value $\simeq 0$). These results imply that similar processes explain the ionization within the high-mass jets, as with their lower mass counterparts (i.e. the shock-ionization models of Curiel et al. 1987). Some jets however have higher fluxes similar to that expected from H II regions (such as G310.1420+00.7583A). This may be explained by a small ionized core at small radii around the MYSO (which is part of the models of Reynolds 1986), existing with the collimated jet contemporaneously, although higher resolution observations would be required to determine this (sub-milliarcsecond for 15 au at a distance of 3 kpc). In such cases, these objects perhaps may represent transition objects between jet and H II phases.

Of the 34 MYSOs from which the DL sample is comprised, we detect a total of 22 objects displaying the characteristics of ionized jets. Of these, 10 (3 of which are candidates) are associated with radio lobes, 10 without (7 of which are candidates) and 2 are ambiguously categorized as jet or disc winds. The mean (and its standard error) bolometric luminosities of isolated jets and jets with lobes are $(2.6 \pm 0.9) \times 10^4 L_{\odot}$ and $(2.7 \pm 1.0) \times 10^4 L_{\odot}$ with medians of 1.8×10^4 and $8.0 \times 10^3 L_{\odot}$, respectively, showing only small differences between the two populations in this respect.

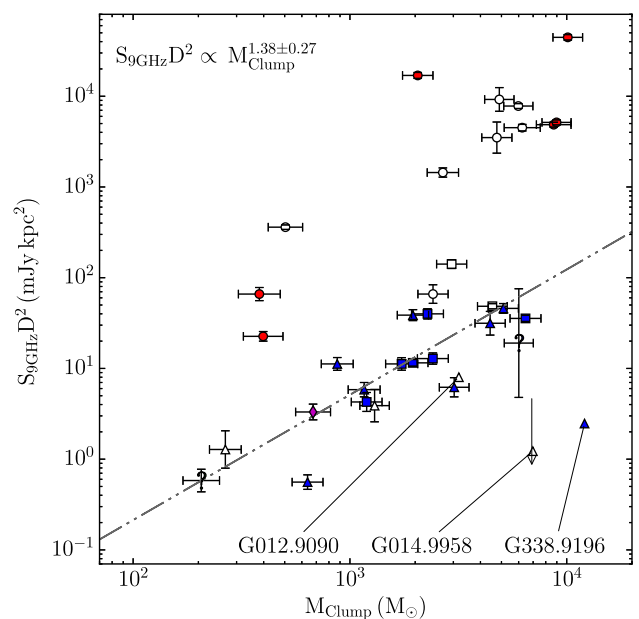


Figure 3. A plot of the 9 GHz distance fluxes against associated clump masses for H II regions and objects displaying properties associated with either ionized jets or disc winds. The coefficient to the fitted power-law fit is displayed in the top-left corner and is represented as the dot-dashed line. Symbols have the same meanings as in Fig. 2.

5.2 9GHz luminosity versus clump mass

An ATLASGAL survey by Urquhart et al. (2014b), recorded the 870 μm fluxes and sizes of a sample of clumps, 35 of which coincide with sources in this survey. We define the term ‘clump’ as being the substructure within giant molecular clouds (GMCs) which ultimately evolve into stellar clusters. In turn, they harbour the smaller substructure of ‘cores’, which are defined as the evolutionary precursor of single (which may or may not display multiplicity) stellar systems (Zinnecker & Yorke 2007). Of those 35 sources, 21 have been classified as exhibiting jet-like characteristics. The clump mass was calculated using the referenced data set in conjunction with the equations of Hildebrand (1983).

In Fig. 3, the radio luminosities at 9 GHz have been plotted against the calculated clump masses and a relation of $S_{\nu}D^2 \propto M_{\text{Clump}}^{1.38 \pm 0.27}$ is derived for all jets and candidates (1.33 ± 0.29 for the jets and candidates from the DL sample). There appears to be two outliers towards the heavier end of the clump masses. G014.9958–00.6732 suffered from elongated beams and noisier data as a result of its observed times. G338.9196+00.5495 is known to be in an extremely active star formation region in general, as well as being located at the edge of its natal clump (see Section 5.5).

Neglecting the two outliers as well as G012.9090–00.2607 (for the same justification as for G014.9958–00.6732), we calculate the correlation coefficient between the clump masses and distance fluxes at 9 GHz (for the DL sample of jets and candidates, neglecting G012.9090–00.2607, G014.9958–00.6732 and G338.9196+00.5495) to be $\tau = 0.63$ with a p -value of 0.002. This indicates a high likelihood of a positive correlation between the two quantities and justifies the empirical power law, fitted in Fig. 3. For the partial Kendall correlation coefficient for distance-flux with clump mass (controlling for distance), we calculate a value of $\tau = 0.55$ with a p -value of 0.009. This statistical result again supports the correlation between jet luminosity and clump

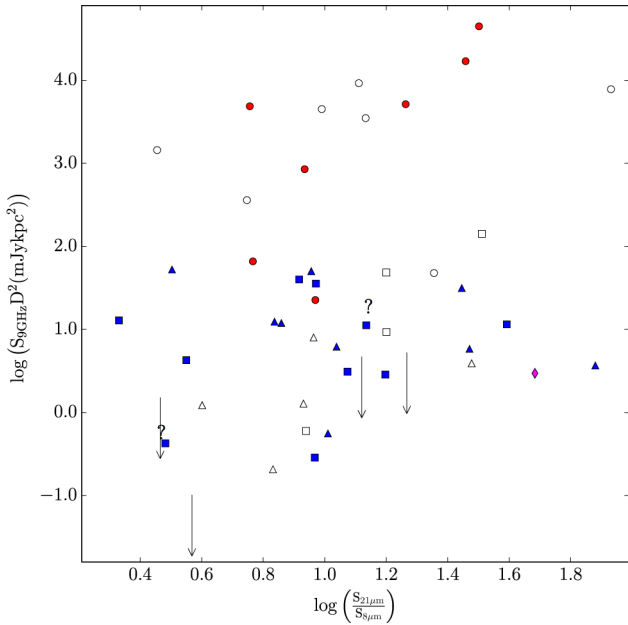


Figure 4. A plot of the logarithm of the 9 GHz fluxes against the MSX 8 μ m/21 μ m colour for the nearest associated MSX point source, for the H II regions and ionized jets detected. Symbols follow the conventions of Fig. 2

mass, as well as the fact that the most massive stars form in the most massive clumps.

As a further note, the two objects classified as unknown are consistent with the fitted power law for the jets and candidates. This provides evidence that these objects may be ionized jets, a classification which higher signal-to-noise observations will help to definitively clarify.

5.3 Radio luminosity versus IR colours

As discussed in Section 2.1, the reddening of sources in infrared surveys can be an accurate indicator of youth since the greater the degree of reddening, the more embedded a source will be in its environment. Extrapolating this reasoning to the MYSO phase, the radio luminosity at 9 GHz has been plotted against the MSX (21–8 μ m) colour in Fig. 4.

While the H II regions appear to show higher radio luminosities with the more reddened mid-infrared colours, the jets show no correlation, holding similar fluxes over the sampled colour-space. This may indicate that the jet phase occupies a relatively large portion of an MYSO’s lifetime. Non-detections occupy the same range of colours as the detected jets themselves. Considering the average bolometric luminosities for the detections and non-detections of the sample are 3.7×10^4 and $3.7 \times 10^3 L_{\odot}$, respectively, the SNR may be insufficient to detect any free-free emission, should it exist coincident with the MSX sources with no detected radio flux. It is also interesting to note that the sources exhibiting disc-wind properties occupy a wide range of colours. However, of these, the unambiguous disc wind (G298.2620+00.7394) holds one of the reddest colours of the jets/disc-winds in the sample. Definite conclusions about whether disc winds represent separate evolutionary stages in MYSO evolution would require a larger sample of such objects than that presented in this work.

5.4 Coincidence with maser and line emission

With regards to the water maser line at 22.23508 GHz, we detect emission within 10 arcsec of 22 of the 42 sources observed in the 22.8 GHz band. Two more of the 42 sources have a detection of water maser activity in previous studies (Forster & Caswell 1999), making a total of 24 of 42 sources. The exact breakdown in terms of object type is summarized in Table 4.

In comparison with the survey by Urquhart et al. (2009b), we find a detection rate of 52 per cent compared to their rate of 27 per cent. This is likely due to the SNR (~ 50 times lower) of this survey since it is continuum oriented (i.e. 1 MHz channels), compared to the previous line oriented study ($4\sigma \sim 1$ Jy). Given the (spectrally) low-resolution nature of continuum observations, no kinematic information could be derived.

5.5 Ionized jets and their general properties

Using equation (5) (Reynolds 1986), it is possible to infer a mass-loss rate in the jet:

$$\dot{M}_{\text{Jet}} = \frac{9.38 \times 10^{-6} v_8 \mu S_{\text{mJy}}^{3/4} d_{\text{kpc}}^{3/2} \theta_0^{3/4}}{x_0 v_{10}^{\alpha} v_{\text{m10}}^{0.45 - \frac{3\alpha}{4}} T_4^{0.075} (\sin i)^{1/4} F^{3/4}}, \quad (5)$$

where α is the derived spectral index, μ is the average particle mass (as a fraction of the proton mass), x_0 is the ionization fraction, v_8 is the terminal velocity of the jet (assumed to be 500 km s $^{-1}$ from proper motion studies in the literature), S_{ν} is the integrated flux density, D is the distance to the source, v_{m10} is the turnover frequency, i is the inclination angle (assumed to be $\sim 39^\circ$), T is the electron temperature and θ_0 is the opening angle at the base of the jet, in radians ($\theta_0 = 2 \tan^{-1}(\theta_{\text{min}}/\theta_{\text{maj}})$). F is given below in equation (6):

$$F \equiv F(q_{\tau}, \alpha) \equiv \frac{4.41}{q_{\tau}(\alpha - 2)(\alpha + 0.1)}, \quad (6)$$

where q_{τ} is the power-law coefficient with which the opacity falls with distance along the jet propagation axis.

Equations (5) and (6) necessitate us to make assumptions for the non-observable parameters contained within them. We assume a higher ionization fraction than in the low-mass case (~ 0.1 ; Hartigan, Morse & Raymond 1994) of 0.2, a typical jet velocity of 500 km s $^{-1}$, (as seen in Section 1 for other examples of ionized jets around MYSOs) and an electron temperature of 10 000 K. For the inclination angle, a value of 39.54° is adopted since the average value for $\sin(i)$ (for uniformly distributed, random inclinations) is found to be ~ 0.64 . These values are used for all of the jets in the sample. The turnover frequency is assumed to be 50 GHz, apart from for the jets whereby $\alpha < 0$, in which case we are already in the optically thin regime and the lowest observed frequency is used. The highest (i.e. most resolving) frequency measurements of the minor/major axes are used in the calculation of the opening angle, for which we find a range between 16° and 80° and a median value of 41° , higher than the range of opening angles found by Moscadelli et al. (2016) towards their sample of MYSOs (10° – 30°), and much greater than typical low-mass cases (5° – 10° ; Tsinganos, Ray & Stute 2009). The widest opening angle was found towards G313.7654–00.8620, which represents a morphologically complex MYSO in the radio, which may have affected the deconvolution (reflected in opening angle errors of 42°). It is important to note at this point that in cases where the opening angle could not be directly measured, we adopted a value of $(20 \pm 15)^\circ$ in line with typical values within the literature.

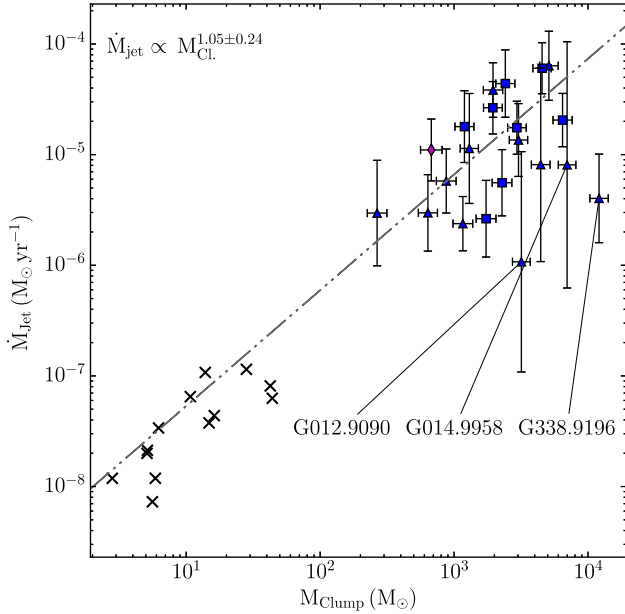


Figure 5. A plot of the inferred mass-loss rates against ATLASGAL derived clump masses (Urquhart et al. 2014b) in the jet for all the sources in our sample displaying jet-like characteristics. The dot-dashed line represents the power-law fit to the data, with the power-law index indicated in the top left of the plot. Data for low-mass jets from Ainsworth et al. (2012) is represented by ‘x’ symbols.

A more complex approach is used when assuming values for q_T . Since (from equation 1) it is dependent on values for ϵ and q_T , we assume one of three models. In the case of $0.4 \leq \alpha < 0.8$, we assume $\epsilon = 1$ and $q_T = 0$, the ‘standard’ spherical model. Where α is measured to be less than 0.4, we assume $\epsilon = 2/3$ and $q_T = 0$, the ‘standard’ collimated model. Finally, in the instances where $\alpha \geq 0.8$, we assign values of $\epsilon = 1$ and $q_T = -0.5$, a conical, recombining jet model.

Derived mass-loss rates range between $(0.3 \text{ and } 64) \times 10^{-6} M_{\odot} \text{ yr}^{-1}$ for all jets/candidates. We calculate a corresponding average mass-loss rate of $(1.5 \pm 0.3) \times 10^{-5} M_{\odot} \text{ yr}^{-1}$, with a median value of $8 \times 10^{-6} M_{\odot} \text{ yr}^{-1}$. Plotting the derived mass-loss rates against the clump masses (Fig. 5) shows a power law with an index of 1.05 ± 0.24 . For this correlation, we calculate $\tau = 0.485$ with an associated p -value of ~ 0.007 . For those objects comprising the DL sample, we calculated $\tau = 0.473$ and a p -value of 0.019. As shown in Table 5, these values do not appreciably change for the partial correlation coefficients, whilst controlling for distance. This confirms that the mass-loss rates in the jets are related to the clump masses, without a distance related bias.

The same three sources were neglected from the correlation tests (G012.9090–00.2607, G014.9958–00.6732 and G338.9196+00.5495) as in Section 5.2. W33A (G012.9090–00.2067) and the Kleinmann–Wright (Kleinmann & Wright 1973) object (G014.9958.00–6732) both lie at declinations conducive to elongated beam shapes, thus adversely affecting their deconvolved sizes. Indeed, W33A was found to have a deconvolved size of $(0.53 \text{ arcsec} \pm 0.14) \times (0.27 \text{ arcsec} \pm 0.11)$ at 43 GHz by van der Tak & Menten (2005), giving an opening angle at the base of the jet of 0.94 rad, in contrast to our derived value of 0.18 rad. This would in turn derive $\dot{M}_{\text{jet}} = (1.7 \pm 1.0) \times 10^{-5} M_{\odot} \text{ yr}^{-1}$ (our derived value is $\sim 1 \times 10^{-6} M_{\odot} \text{ yr}^{-1}$). W33A is also known to be composed of at least three separate sources at very high resolutions, Q1, Q2 and

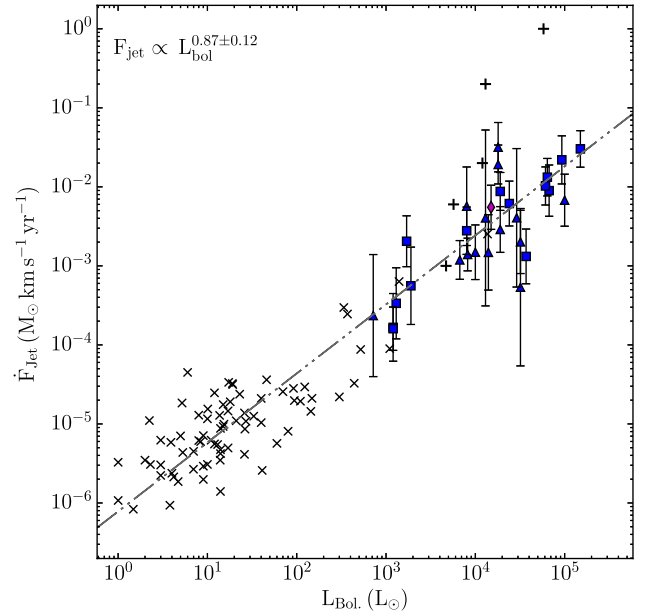


Figure 6. A plot of the inferred momentum rate against bolometric luminosity for the sources in our sample displaying jet-like characteristics. The dot-dashed line represents the power-law fit to the data, with the power-law index indicated in the top left of the plot. Data for low-mass jets from Ainsworth et al. (2012) is represented by ‘x’ symbols, assuming a velocity of 200 km s^{-1} unless otherwise indicated in the literature. The ‘+’ symbol indicates data for the high-mass sample from Moscadelli et al. (2016).

Q3 (Q1 represents the main jet). This complicates the analysis, requiring higher resolutions observations (at all frequencies) in order to separate and determine the natures of each source.

The KW object is positioned at the edges of two ATLASGAL ($R_{\text{eff}} \sim 60 \text{ arcsec}$ and $R_{\text{eff}} \sim 90 \text{ arcsec}$) clumps, the membership to which is uncertain. If the accretion, and hence jet mass-loss rates, are intrinsically tied to the reservoir of material from the clump, this may explain (in combination with the elongated beam) its current (relatively low) mass-loss rate of $\sim 4 \times 10^{-6} M_{\odot} \text{ yr}^{-1}$.

G338.9196+00.5495 images had low SNR, showed the presence of five HCHII/UCHIIs within 1 arcmin of the source, and displayed partially resolved out extended emission at the lowest frequencies. The busy nature of the environment would affect the reservoir of available material to the MYSO and hence affect jet outflow rates, as well as the quality of the images and deconvolved dimensions of the object itself (which is unresolved at 17 and 22.8 GHz). ATLASGAL images of G338.9196+00.5495 also show its parental clump to be comprised of two, non-resolved clumps, with the source offset on the southern edge of the smaller, thus the clump’s mass may be overestimated. Considering that G338.9196+00.5495 is also an outlier in Fig. 3, it is likely that the clump mass is poorly constrained as discussed above.

As a check with the rest of the data, all sources apart from the KW object, G338.9196+00.5495 and G345.9561+00.6123 (which is still of uncertain classification) are positioned within the inner 25 per cent of their parental clumps (cf. Urquhart et al. 2014b, who found 90 per cent of embedded objects were separated by less than 0.5 pc from their associated clump’s peak flux position).

Inferred momentum rates (assuming a terminal velocity for the jet of 500 km s^{-1}) against the bolometric luminosities of the powering sources, are plotted in Fig. 6. We find the relation presented in

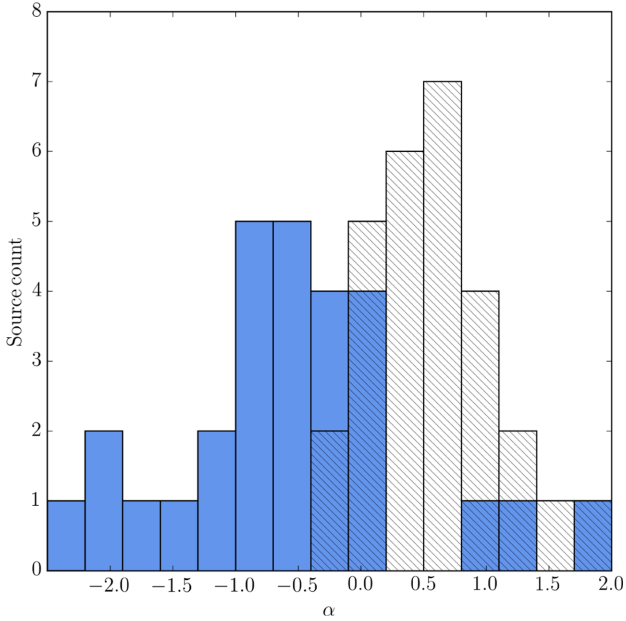


Figure 7. A histogram of all the spectral indices derived for those sources determined to exhibit jet-like characteristics (hatched). The solid blue bars are for the associated lobes. Binning starts at $\alpha = -2.5$ and bin widths are set at 0.3 due to the sample size.

equation (7) for those sources comprising the DL sample (derived values change little between jet and jet/candidate subsamples). Comparing this to the CO outflow momentum rate/bolometric luminosity relations found by Cabrit & Bertout (1992, equation 8) and Maud et al. (2015, equation 9):

$$\log_{10} F_{\text{jet}} = (-6.11 \pm 0.49) + (0.87 \pm 0.12) \log_{10} L_{\text{bol}} \quad (7)$$

$$\log_{10} F_{\text{CO}} = (-4.36 \pm 0.12) + (0.69 \pm 0.05) \log_{10} L_{\text{bol}} \quad (8)$$

$$\log_{10} F_{\text{CO}} = (-4.60 \pm 0.46) + (0.61 \pm 0.11) \log_{10} L_{\text{bol}}. \quad (9)$$

Within errors, the momentum rate of ionized jets appears to depend more heavily on the bolometric luminosities than the molecular outflows. However, the incidence rate of massive molecular outflows in the (6 kpc DL) MYSO sample of Maud et al. (2015) was found to be 66 percent, similar to the incidence rate of jets and candidates for our DL sample of 65 percent. The power-law coefficient for the relation between the molecular mass outflow rate and clump mass was found to be 0.55 ± 0.10 . In comparison to our fitted value of 1.06 ± 0.24 for the jet outflow rate, this indicates a heavier dependence of the outflow rates on the clump mass for ionized jets, than for the molecular outflows.

In Fig. 7, the histogram of the spectral indices derived for all jets in our sample is presented. This shows a peak in the jet's spectral indices of ~ 0.6 as per the standard, conical jet model. All detected jets exhibit spectral indices expected from the models of Reynolds (1986) between -0.1 and 1.6 within errors. As for the lobes of emission associated with the thermal jets, we derive non-thermal spectral indices for lobes associated with 10 of the 13 jets. An average spectral index in the non-thermal lobes of -0.55 is also calculated showing that synchrotron emission is the dominant emission mechanism in these cases and therefore magnetic fields are present in the environments of ionized jets from MYSOs. This result also agrees with radio lobes being produced via *Fermi* acceleration at shocks, whereby we expect $\alpha = (1 - p)/2$, where p is the power-law

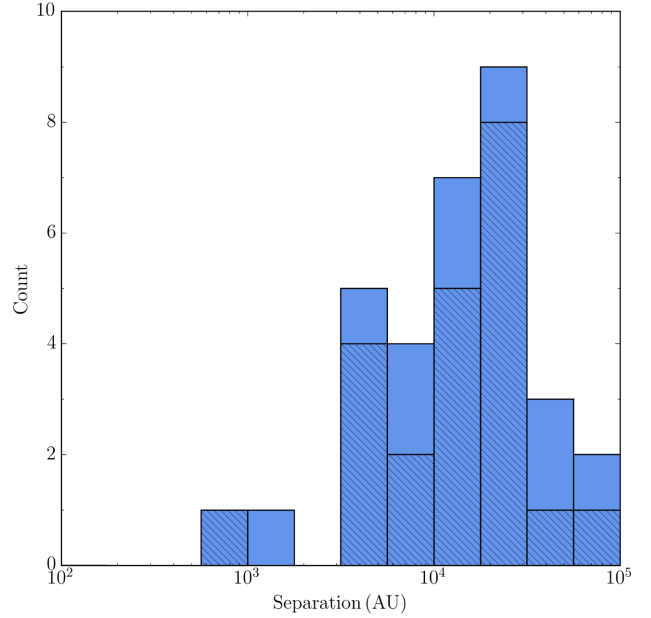


Figure 8. A logarithmic histogram of the spatial separations between all lobes (solid bars), and lobes where $\alpha < 0$ (hatched bars), and their powering central jets.

coefficient for the electron energy distribution ($p = 2$ in head-on shocks). Four of the jets show associated lobes with thermal spectral indices, G310.0135+00.3892 (SW), G310.1420+00.7583A (B), G313.7654−00.8620 (B2) and G332.0939−00.4206 (E). For all four cases, apart from G313.7654−00.8620, the spectra of the components are not well fitted by simple power laws suggesting these components may represent extended emission (i.e. resolved out at higher frequencies), the natures of which are indeterminate. G313.7654−00.8620 was observed at the lower two frequencies only, and so the presence of this effect is unknown, raising another possibility of multiplicity. For the SW component of G310.0135+00.3892, the alignment between the central radio source and this component is parallel to derived outflow directions in the literature. Therefore, it is likely this represents thermal emission from the jet material however more sensitive observations with higher signal to noise are required to conclude this definitively.

For those jets identified which had associated lobes of emission, the separation of these lobes from the central jet was calculated (assuming an inclination of 90°) and in Fig. 8, the histogram of logarithmic lobe separations is plotted. A peak in the separations at $\sim 10^4$ au from the central object is evident, with a mean value of 2.0×10^4 au (and a median value of 1.3×10^4 au). The minimum separation calculated (~ 600 au) was for the NW component of G263.7759−00.4281, while the maximum ($\sim 90\,000$ au) was for component D of G313.7654−00.8620. If these lobes represent internal shocks within the jet as a result of periodic ejection coupled with non-constant ejection velocities, we can calculate the typical time between these ejections. Assuming an ejection velocity of 500 km s^{-1} for the first ejection, which increases by 10 per cent for the second, and using the typical value for lobe separations of 1.3×10^4 au, it can be inferred that the time between these ejections is typically ~ 10 yr.

It is important to note that the population of small separation lobes is undersampled and we cannot reliably comment on lobe separations for distances < 4000 au, due to the minimum resolvable scales of the observations. In order to investigate the spectral consequences

of this resolution limit, we analysed the spectral indices for the combined fluxes of north and south lobes, for both G263.7434+00.1161 and G310.0135+00.3892 (due to their relative morphological simplicities). Derived values for the spectral index of the combined emission were found to be $\alpha = 0.09 \pm 0.13$ and $\alpha = 0.42 \pm 0.17$ for G263.7434+00.1161 and G310.0135+00.3892 (for the thermal jets alone, $\alpha = 0.39 \pm 0.18$ and $\alpha = 1.27 \pm 0.18$), respectively, with the combined fluxes being fitted well with a simple power law. This indicates that any unresolved, optically thin lobes which are inseparable from their powering, thermal jets, would flatten the jet's spectrum without strongly distorting its power-law profile. This effect could act to decrease the measured spectral index for jets, whose flux incorporates those of optically thin or non-thermal lobes, offering another explanation for a slightly larger proportion of jets with spectral indices <0.6 (see Fig. 7).

5.6 H II regions and their general properties

From the H II regions that were included in the overall sample, we have calculated both the emission measures and physical radii (deconvolved). The three HCHII regions displaying a compact core have been separated from their extended background emission, with both components analysed separately. Both emission measures and radii are plotted in Fig. 9.

For the HCHII regions in our sample, we find an average emission measure of $6.51 \times 10^8 \text{ pc cm}^{-6}$ and corresponding electron density of $2.28 \times 10^5 \text{ cm}^{-3}$. For the ultracompact H II regions detected, we find values of $1.09 \times 10^8 \text{ pc cm}^{-6}$ and $5.13 \times 10^4 \text{ cm}^{-3}$ for the average emission measure and electron density. Average radii were calculated to be 0.013 and 0.041 pc, while average bolometric luminosities were calculated to be $(1.6 \pm 0.4) \times 10^5 L_{\odot}$ and $(7.9 \pm 1.1) \times 10^4 L_{\odot}$, for HCHII and UCHII, respectively (assuming a 34 per cent error in the bolometric luminosities, as in Mottram et al. 2011). Although H II regions are not the focus of this paper, the derived properties provide a consistency check for typical values reported in the literature (Mezger et al. 1967; Wood & Churchwell 1989; Hoare et al. 2007).

6 CONCLUSIONS

In this work, we present the results of radio observations made towards 49 MYSOs potentially harbouring ionized jets, 34 of which form a DL sample. Our goal is to establish how common this phenomenon is for the formation process of massive stars, the relation to possible accretion processes/models and the physical parameters typical of the jets themselves. In summary, our main results and conclusions are as follows.

(i) From the DL sample of 34 MYSOs, we detect 22 ionized jets and jet candidates showing this to be a common phenomenon in forming massive stars. Disc based accretion processes are therefore the dominant mechanism of accretion (up to masses of at least $25 M_{\odot}$).

(ii) Ionized jets are more common than disc winds, by at least an order of magnitude. This suggests that either ionized jets are generally brighter than disc winds (if they are concurrent), or that a distinct disc-wind phase exists and is relatively short in comparison.

(iii) Assuming an MYSO phase lifetime of $\sim 10^5$ yr (McKee & Tan 2002), a jet-phase lasting $(2.9\text{--}6.5) \times 10^4$ yr is implied from the incidence rate of jets and jet candidates. Since some objects potentially represent a transition phase between ionized jet and H II region, this time range is placed at the later end of an MYSO's

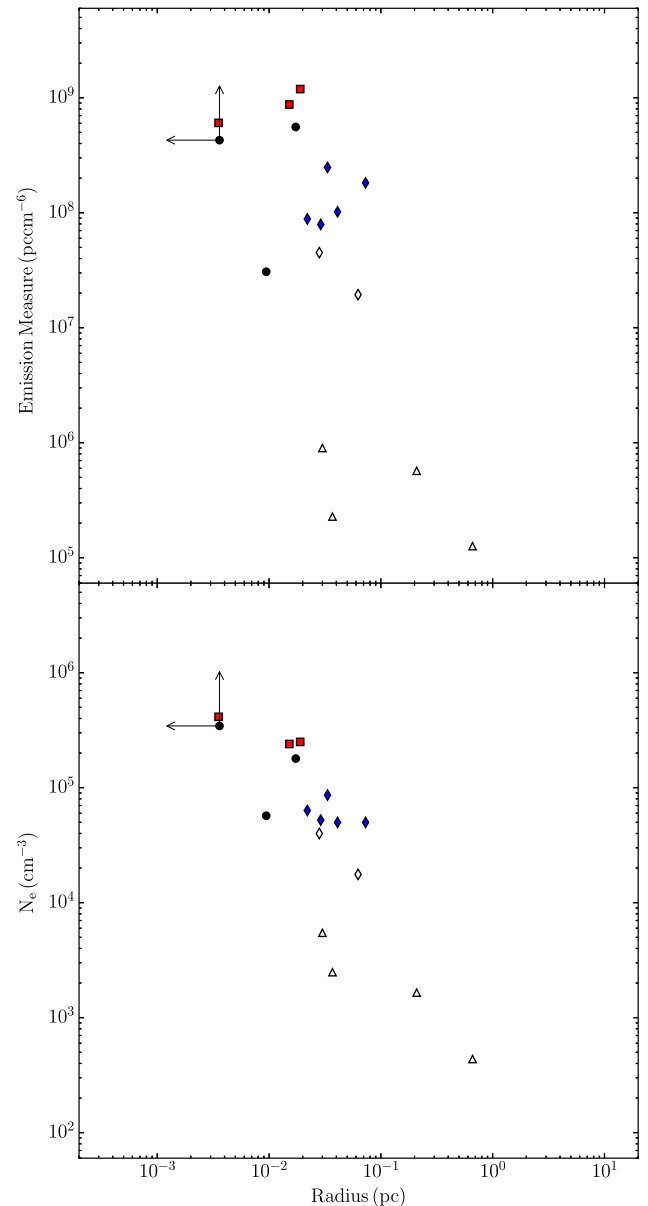


Figure 9. A plot of the calculated emission measures against radius for the H II regions detected in our sample (top) and the corresponding electron densities inferred against radius (bottom). Circles (black) represent the compact HCHII ‘core’ seen in three H II regions, squares (red) represent other HCHII regions, diamonds (blue) represent UCHII regions, and triangles represent compact and classical H II regions. Any symbols in white suffer from resolving out effects due to their scale.

lifetime, implying accretion does not completely halt after the initial production of an H II region.

(iv) The luminosity and momenta of our sample of massive, ionized jets scale with bolometric luminosity in the same way as low-mass jets, supporting the idea that these jets are produced in the same way over YSO mass ranges up to at least $25 M_{\odot}$.

(v) Typical jet mass-loss rates and momenta rates are $1.4 \times 10^{-5} M_{\odot} \text{ yr}^{-1}$ and $0.7 \times 10^{-2} M_{\odot} \text{ km s}^{-1} \text{ yr}^{-1}$, respectively, assuming an average ionization fraction of 20 per cent and jet velocity of 500 km s^{-1} . This suggests an average mass of $\sim 1\text{--}2 M_{\odot}$ (corresponding to $\sim 10^{48}$ erg) is lost through the ionized jet mechanism, to the ISM, over the course of an MYSO’s jet-phase.

(vi) Jet outflow rates (and hence accretion rates) are closely related to the mass of the molecular clump from which they form, which agrees with the idea that the most massive stars form in the most massive clumps. This is also supported by the fact that 88 per cent of the jets are found in the inner 25 per cent of their associated clump.

(vii) Synchrotron emission is commonplace (present in ~75 per cent of the jets displaying associated lobes) and as a result, this lends support to the idea of magnetic collimation in ionized jets around MYSOs, as in the low-mass case.

ACKNOWLEDGEMENTS

We thank the referee for constructive comments. SJDJ gratefully acknowledges the studentship funded by the Science and Technology Facilities Council of the United Kingdom (STFC). AEG acknowledges support from FONCEDYT grant 3150570. The National Radio Astronomy Observatory is a facility of the National Science Foundation operated under cooperative agreement by Associated Universities, Inc. This paper has made use of information from the RMS survey data base at <http://www.ast.leeds.ac.uk/RMS> which was constructed with support from the Science and Technology Facilities Council of the United Kingdom.

REFERENCES

- Ainsworth R. E., Scaife A. M. M., Shimwell T., Titterton D., Waldram E., 2012, *MNRAS*, 423, 1089
- Anglada G., 1995, *Rev. Mex. Astron. Astrofis. Ser. Conf.*, 1, 67
- Anglada G., Villuendas E., Estalella R., Beltrán M. T., Rodríguez L. F., Torrelles J. M., Curiel S., 1998, *ApJ*, 116, 2953
- Arce H. G., Shepherd D., Gueth F., Lee C.-F., Bachiller R., Rosen A., Beuther H., 2007, in Reipurth B., Jewitt D., Keil K., eds, *Protostars and Planets V*. Univ. Arizona Press, Tucson, AZ, p. 245
- Barres de Almeida U., Abraham Z., Roman-Lopes A., 2006, *Mem. Soc. Astron. Ital.*, 77, 1158
- Beuther H., Schilke P., Sridharan T. K., Menten K. M., Walmsley C. M., Wyrowski F., 2002, *A&A*, 383, 892
- Blandford R. D., Payne D. G., 1982, *MNRAS*, 199, 883
- Bonnell I. A., Bate M. R., Clarke C. J., Pringle J. E., 2001, *MNRAS*, 323, 785
- Bornancini C. G., O'Mill A. L., Gurovich S., Lambas D. G., 2010, *MNRAS*, 406, 197
- Burkert A., Stecklum B., Henning T., Fischer O., 2000, *A&A*, 353, 153
- Cabrit S., Bertout C., 1992, *A&A*, 261, 274
- Campbell B., 1984, *ApJ*, 282, L27
- Caratti o Garatti A., Stecklum B., Linz H., Garcia Lopez R., Sanna A., 2015, *A&A*, 573, A82
- Carrasco-González C., Rodríguez L. F., Anglada G., Martí J., Torrelles J. M., Osorio M., 2010, *Science*, 330, 1209
- Carrasco-González C. et al., 2012, *ApJ*, 752, L29
- Carrasco-González C. et al., 2015, *Science*, 348, 114
- Caswell J. L., 1998, *MNRAS*, 297, 215
- Cesaroni R., Galli D., Lodato G., Walmsley C. M., Zhang Q., 2007, in Reipurth B., Jewitt D., Keil K., eds, *Protostars and Planets V*. Univ. Arizona Press, Tucson, AZ, p. 197
- Chini R., Hoffmeister V. H., Kämpgen K., Kimeswenger S., Nielbock M., Siebenmorgen R., 2004, *A&A*, 427, 849
- Curiel S., Canto J., Rodríguez L. F., 1987, *Rev. Mex. Astron. Astrofis.*, 14, 595
- Curiel S. et al., 2006, *ApJ*, 638, 878
- Cyganowski C. J. et al., 2008, *ApJ*, 136, 2391
- Davies B., Lumsden S. L., Hoare M. G., Oudmaijer R. D., de Wit W.-J., 2010, *MNRAS*, 402, 1504
- Davies B., Hoare M. G., Lumsden S. L., Hosokawa T., Oudmaijer R. D., Urquhart J. S., Mottram J. C., Stead J., 2011, *MNRAS*, 416, 972
- De Buizer J. M., 2003, *MNRAS*, 341, 277
- De Buizer J. M., Walsh A. J., Piña R. K., Phillips C. J., Telesco C. M., 2002, *ApJ*, 564, 327
- De Buizer J. M., Redman R. O., Longmore S. N., Caswell J., Feldman P. A., 2009, *A&A*, 493, 127
- de Luca M., Giannini T., Lorenzetti D., Massi F., Elia D., Nisini B., 2007, *A&A*, 474, 863
- Eisloffel J., Mundt R., Ray T. P., Rodriguez L. F., 2000, in Mannings V., Boss A.P., Russell S. S., eds, *Protostars and Planets IV*. Univ. Arizona Press, Tucson, AZ, p. 815
- Ellingsen S. P., 2006, *ApJ*, 638, 241
- Ellingsen S. P., Norris R. P., McCulloch P. M., 1996, *MNRAS*, 279, 101
- Felli M., Taylor G. B., Neckel T., Staude H. J., 1998, *A&A*, 329, 243
- Fernández-López M., Curiel S., Girart J. M., Ho P. T. P., Patel N., Gómez Y., 2011, *ApJ*, 141, 72
- Forster J. R., Caswell J. L., 1989, *A&A*, 213, 339
- Forster J. R., Caswell J. L., 1999, *A&AS*, 137, 43
- Frater R. H., Brooks J. W., Whiteoak J. B., 1992, *J. Electr. Electron. Eng. Aust.*, 12, 103
- Furuya R. S., Kitamura Y., Wootten A., Claussen M. J., Kawabe R., 2003, *ApJS*, 144, 71
- Galván-Madrid R., Zhang Q., Keto E., Ho P. T. P., Zapata L. A., Rodríguez L. F., Pineda J. E., Vázquez-Semadeni E., 2010, *ApJ*, 725, 17
- Garay G., Brooks K. J., Mardones D., Norris R. P., 2003, *ApJ*, 587, 739
- Garay G. et al., 2007, *A&A*, 463, 217
- Giannini T. et al., 2005, *A&A*, 433, 941
- Giannini T. et al., 2013, *ApJ*, 767, 147
- Gibb A. G., Hoare M. G., 2007, *MNRAS*, 380, 246
- Green J. A. et al., 2012, *MNRAS*, 420, 3108
- Guzmán A. E., Garay G., Brooks K. J., 2010, *ApJ*, 725, 734
- Guzmán A. E., Garay G., Brooks K. J., Rathborne J., Güsten R., 2011, *ApJ*, 736, 150
- Guzmán A. E., Garay G., Brooks K. J., Voronkov M. A., 2012, *ApJ*, 753, 51
- Guzmán A. E. et al., 2014, *ApJ*, 796, 117
- Hartigan P., Morse J. A., Raymond J., 1994, *ApJ*, 436, 125
- Henning T., Schreyer K., Launhardt R., Burkert A., 2000a, *A&A*, 353, 211
- Henning T., Lapinov A., Schreyer K., Stecklum B., Zinchenko I., 2000b, *A&A*, 364, 613
- Higuchi A. E., Saigo K., Chibueze J. O., Sanhueza P., Takakuwa S., Garay G., 2015, *ApJ*, 798, L33
- Hildebrand R. H., 1983, *QJRAS*, 24, 267
- Hoare M. G., Kurtz S. E., Lizano S., Keto E., Hofner P., 2007, in Reipurth B., Jewitt D., Keil K., eds, *Protostars and Planets V*. Univ. Arizona Press, Tucson, AZ, p. 181
- Hollenbach D., McKee C. F., 1989, *ApJ*, 342, 306
- Hosokawa T., Omukai K., 2009, *ApJ*, 691, 823
- Ilee J. D. et al., 2013, *MNRAS*, 429, 2960
- Jackson C. A., 2004, *New Astron. Rev.*, 48, 1187
- Kendall M. G., 1938, *Biometrika*, 30, 81
- Kleinmann D. E., Wright E. L., 1973, *ApJ*, 185, L131
- Kraus S. et al., 2010, *Nature*, 466, 339
- Lee J.-K., Walsh A. J., Burton M. G., Ashley M. C. B., 2001, *MNRAS*, 324, 1102
- Linz H., Hofner P., Araya E., Rodríguez L. F., Kurtz S., Martí J., Stecklum B., Henning T., 2004, *Astron. Nachr.*, 325, 11
- Lizano S., 2008, in Beuther H., Linz H., Henning T., eds, *ASP Conf. Ser. Vol. 387, Massive Star Formation: Observations Confront Theory*. Astron. Soc. Pac., San Francisco, p. 232
- Lumsden S. L., Hoare M. G., Oudmaijer R. D., Richards D., 2002, *MNRAS*, 336, 621
- Lumsden S. L., Hoare M. G., Urquhart J. S., Oudmaijer R. D., Davies B., Mottram J. C., Cooper H. D. B., Moore T. J. T., 2013, *ApJS*, 208, 11
- McKee C. F., Tan J. C., 2002, *Nature*, 416, 59
- McMullin J. P., Waters B., Schiebel D., Young W., Golap K., 2007, in Shaw R. A., Hill F., Bell D. J., eds, *ASP Conf. Ser. Vol. 376, Astronomical Data*

- Analysis Software and Systems XVI. Astron. Soc. Pac., San Francisco, p. 127
- Marti J., Rodríguez L. F., Reipurth B., 1993, *ApJ*, 416, 208
- Marti J., Rodríguez L. F., Reipurth B., 1995, *ApJ*, 449, 184
- Martí J., Rodríguez L. F., Reipurth B., 1998, *ApJ*, 502, 337
- Maud L. T., Moore T. J. T., Lumsden S. L., Mottram J. C., Urquhart J. S., Hoare M. G., 2015, *MNRAS*, 453, 645
- Mezger P. G., Altenhoff W., Schraml J., Burke B. F., Reifenstein E. C., III, Wilson T. L., 1967, *ApJ*, 150, L157
- Miettinen O., Harju J., Haikala L. K., Pomrén C., 2006, *A&A*, 460, 721
- Moscadelli L. et al., 2016, *A&A*, 585, A71
- Mottram J. C., Hoare M. G., Lumsden S. L., Oudmaijer R. D., Urquhart J. S., Sheret T. L., Clarke A. J., Allsopp J., 2007, *A&A*, 476, 1019
- Mottram J. C., Hoare M. G., Lumsden S. L., Oudmaijer R. D., Urquhart J. S., Meade M. R., Moore T. J. T., Stead J. J., 2010, *A&A*, 510, A89
- Mottram J. C. et al., 2011, *A&A*, 525, A149
- Navarete F., Damineli A., Barbosa C. L., Blum R. D., 2015, *MNRAS*, 450, 4364
- Neckel T., Staude H. J., 1995, *ApJ*, 448, 832
- Patel N. A. et al., 2005, *Nature*, 437, 109
- Phillips C. J., Norris R. P., Ellingsen S. P., McCulloch P. M., 1998, *MNRAS*, 300, 1131
- Povich M. S. et al., 2009, *ApJ*, 696, 1278
- Price S. D., Egan M. P., Carey S. J., Mizuno D. R., Kuchar T. A., 2001, *ApJ*, 121, 2819
- Rengarajan T. N., Ho P. T. P., 1996, *ApJ*, 465, 363
- Reynolds S. P., 1986, *ApJ*, 304, 713
- Rodríguez L. F., Garay G., Curiel S., Ramirez S., Torrelles J. M., Gomez Y., Velazquez A., 1994, *ApJ*, 430, L65
- Rodríguez L. F., Garay G., Brooks K. J., Mardones D., 2005, *ApJ*, 626, 953
- Rodríguez L. F., Moran J. M., Franco-Hernández R., Garay G., Brooks K. J., Mardones D., 2008, *ApJ*, 135, 2370
- Rodríguez L. F., González R. F., Montes G., Asiri H. M., Raga A. C., Cantó J., 2012, *ApJ*, 755, 152
- Sandell G., Goss W. M., Wright M., Corder S., 2009, *ApJ*, 699, L31
- Sault R. J., Wieringa M. H., 1994, *A&AS*, 108, 585
- Sault R. J., Teuben P. J., Wright M. C. H., 1995, in Shaw R. A., Payne H. E., Hayes J. J. E., eds, *ASP Conf. Ser. Vol. 77, Astronomical Data Analysis Software and Systems IV*. Astron. Soc. Pac., San Francisco, p. 433
- Scaife A. M. M. et al., 2011, *MNRAS*, 415, 893
- Seifried D., Pudritz R. E., Banerjee R., Duffin D., Klessen R. S., 2012, *MNRAS*, 422, 347
- Shu F. H., Adams F. C., Lizano S., 1987, *ARA&A*, 25, 23
- Shu F., Najita J., Ostriker E., Wilkin F., Ruden S., Lizano S., 1994, *ApJ*, 429, 781
- Smith M. D., Rosen A., 2005, *MNRAS*, 357, 1370
- Stahler S. W., 1988, *ApJ*, 332, 804
- Stecklum B., Kauff H., 1998, *ESO Press Release*
- Stecklum B., Caratti o Garatti A., Linz H., 2012, in Carciofi A. C., Rivinius T., eds, *ASP Conf. Ser. Vol. 464, Circumstellar Dynamics at High Resolution*. Astron. Soc. Pac., San Francisco, p. 369
- Thi W.-F., van Dishoeck E. F., Pontoppidan K. M., Dartois E., 2010, *MNRAS*, 406, 1409
- Thompson R. I., 1984, *ApJ*, 283, 165
- Tsinganos K., Ray T., Stute M., 2009, *Proc. Astrophys. Space Sci., Protostellar Jets in Context*. Springer-Verlag, Berlin
- Urquhart J. S., Busfield A. L., Hoare M. G., Lumsden S. L., Clarke A. J., Moore T. J. T., Mottram J. C., Oudmaijer R. D., 2007, *A&A*, 461, 11
- Urquhart J. S. et al., 2007, *A&A*, 474, 891
- Urquhart J. S. et al., 2009a, *A&A*, 501, 539
- Urquhart J. S. et al., 2009b, *A&A*, 507, 795
- Urquhart J. S., Figura C. C., Moore T. J. T., Hoare M. G., Lumsden S. L., Mottram J. C., Thompson M. A., Oudmaijer R. D., 2014a, *MNRAS*, 437, 1791
- Urquhart J. S. et al., 2014b, *MNRAS*, 443, 1555
- van der Tak F. F. S., Menten K. M., 2005, *A&A*, 437, 947
- Voronkov M. A., Caswell J. L., Ellingsen S. P., Green J. A., Breen S. L., 2014, *MNRAS*, 439, 2584
- Walsh A. J., Burton M. G., Hyland A. R., Robinson G., 1998, *MNRAS*, 301, 640
- Wheelwright H. E., de Wit W. J., Oudmaijer R. D., Hoare M. G., Lumsden S. L., Fujiyoshi T., Close J. L., 2012, *A&A*, 540, A89
- Wilson W. E., Ferris R. H., Axtens P., Brown A., Davis E., Hampson G., Leach M., Roberts P., 2011, *MNRAS*, 416, 832
- Wolfire M. G., Konigl A., 1991, *ApJ*, 383, 205
- Wood D. O. S., Churchwell E., 1989, *ApJS*, 69, 831
- Wood D. O. S., Handa T., Fukui Y., Churchwell E., Sofue Y., Iwata T., 1988, *ApJ*, 326, 884
- Yu N., Wang J.-J., 2014, *MNRAS*, 440, 1213
- Zapata L. A., Palau A., Galván-Madrid R., Rodríguez L. F., Garay G., Moran J. M., Franco-Hernández R., 2015, *MNRAS*, 447, 1826
- Zinnecker H., Yorke H., 2007, *ARA&A*, 45, 481

SUPPORTING INFORMATION

Additional Supporting Information may be found in the online version of this article:

Appendix A. Tables.

Appendix B. Discussion of individual targets.

Appendix C. Figures.

(<http://www.mnras.oxfordjournals.org/lookup/suppl/doi:10.1093/mnras/stw1027/-/DC1>).

Please note: Oxford University Press is not responsible for the content or functionality of any supporting materials supplied by the authors. Any queries (other than missing material) should be directed to the corresponding author for this article.

This paper has been typeset from a $\text{\TeX}/\text{\LaTeX}$ file prepared by the author.